Draft version September 7, 2022
Typeset using LaTeX **twocolumn** style in AASTeX62

Discovery of an Ultra Lithium-rich Metal-Poor Red Giant star

Jeremy Kowkabany,[1,2] Rana Ezzeddine,[1,3] Corinne Charbonnel,[4,5] Ian U. Roederer,[6,3] Yangyang Li,[1] Zoe Hackshaw,[7] Timothy C. Beers,[8,3] Anna Frebel,[9,3] Terese T. Hansen,[10] Erika Holmbeck,[11,12,3] Vinicius M. Placco,[13] and Charli M. Sakari[14]

[1] *Department of Astronomy, University of Florida, Gainesville, FL 32601, USA*
[2] *Department of Physics, Florida State University, Tallahassee, FL 32306, USA*
[3] *Joint Institute for Nuclear Astrophysics - Center for Evolution of the Elements, USA*
[4] *Department of Astronomy, University of Geneva, Chemin de Pégase 51, 1290 Versoix, Switzerland*
[5] *IRAP, CNRS UMR 5277 & Université de Toulouse, 14 av. E. Belin, 31400 Toulouse, France*
[6] *Department of Astronomy, University of Michigan, Ann Arbor, MI 48109, USA*
[7] *Department of Astronomy, University of Texas at Austin, 2515 Speedway, Austin, Texas 78712-1205, USA*
[8] *Department of Physics and Astronomy, University of Notre Dame, Notre Dame, IN 46556, USA*
[9] *Department of Physics & Kavli Institute for Astrophysics and Space Research, Massachusetts Institute of Technology, Cambridge, MA 02139, USA*
[10] *Department of Astronomy, Stockholm University, AlbaNova University Centre, SE-106 91 Stockholm, Sweden*
[11] *Observatories of the Carnegie Institution for Science, Pasadena, CA 91101, USA*
[12] *Hubble Fellow*
[13] *NSF's NOIRLab, 950 N. Cherry Ave., Tucson, AZ 85719, USA*
[14] *San Francisco State University, 1600 Holloway Avenue, San Francisco, CA, 94132 USA*

ABSTRACT

We present the discovery of 2MASS J05241392−0336543 (hereafter J0524−0336), a very metal-poor ([Fe/H]= -2.43 ± 0.16), highly r-process-enhanced ([Eu/Fe]= $+1.34 \pm 0.10$) Milky Way halo field red giant star, with an ultra high Li abundance of A(Li)(3D,NLTE)= 5.62 ± 0.25 and [Li/Fe]= $+7.00 \pm 0.25$, respectively. This makes J0524−0336 the most lithium-enhanced giant star discovered to date. We present a detailed analysis of the star's atmospheric stellar parameters and chemical-abundance determinations. Additionally, we detect infrared excess and variable emission in the wings of the H_α absorption line across multiple epochs, indicative of a potential enhanced mass-loss event with possible outflows. Our analysis reveals that J0524−0336 lies either between the bump and the tip of the Red Giant Branch (RGB), or on the early-Asymptotic Giant Branch (e-AGB). We investigate the possible sources of lithium enrichment in J0524−0336, including both internal and external sources. Based on current models and on the observational evidence we have collected, our study shows that J0524−0336 may be undergoing the so-called *lithium flash* that is expected to occur in low-mass stars when they reach the RGB bump and/or the early-AGB.

Keywords: lithium — stars: abundances — stars: AGB — stars: r-process

1. INTRODUCTION

Observational evidence has accumulated on the decrease of the *lithium* (Li) photospheric abundance in low-mass stars (LMS) as they age. Li depletion is observed to occur already on the pre-main sequence for the very low-mass stars, and along the main sequence with mass and age-dependent efficiency that can not be explained by so-called classical stellar-evolution models (e.g., Charbonneau & Michaud 1990; Soderblom et al. 1993; Lyubimkov 2016; Tognelli et al. 2021; Binks et al. 2022). The observed Li patterns instead reveal the occurrence of internal transport processes of chemical elements other than convection in LMS (e.g., Deliyannis et al. 2000; Talon & Charbonnel 2010). Models including atomic diffusion and turbulence are almost fully bridging the gap between the primordial (BBN) Li abundance and the Li observed in metal-poor warm turnoff stars along the Spite plateau and in globular clusters

Corresponding author: Rana Ezzeddine
rezzeddine@ufl.edu

(e.g., Richard et al. 2005; Korn et al. 2006; Nordlander et al. 2012; Gruyters et al. 2016; Deal & Martins 2021). Also, the Li depletion in more metal-rich stars like the Sun and F- and G-type dwarfs in open clusters can be self-consistently reproduced when accounting for different hydrodynamical processes that transport both matter and angular momentum in stellar interiors (e.g., Charbonnel & Talon 2005; Dumont et al. 2021a,b, and references therein).

The photospheric Li keeps decreasing during the so-called first dredge-up (FDU) when LMS evolve towards the red giant branch (RGB; e.g., Iben 1967), as evidenced both in metal-poor stars from the halo and globular clusters and in metal-rich stars in the field and in open clusters (e.g., Lèbre et al. 1999; Charbonnel et al. 2000; Charbonnel et al. 2020; Lind et al. 2009; Canto Martins et al. 2011; Magrini et al. 2021a; Aguilera-Gómez et al. 2022; Mucciarelli et al. 2022). Later, Li decreases again sharply as soon as the stars reach the luminosity of the bump on the upper RGB (e.g., Charbonnel et al. 1998; Gratton et al. 2000; Lind et al. 2009; Charbonnel et al. 2020). This last Li depletion episode is well reproduced by stellar evolution models including simplistic prescriptions for the so-called thermohaline mixing, a double diffusive process which connects the base of the convective envelope to the hydrogen-burning shell of low-mass red giants and decreases their photospheric Li abundance and carbon isotopic ratio simultaneously (Charbonnel & Zahn 2007; Charbonnel & Lagarde 2010). Given the universality of the FDU in low mass stellar evolution, and the sensitivity of lithium to mixing processes as evidenced for both metal-poor and metal-rich dwarf and giant stars, one could reasonably expect to observe low lithium abundance in all low-mass giant stars, independently of their initial metal-content. While this is generally the case, a small fraction of low-mass red giants exhibit exceptionally high Li abundances.

The enhancement of lithium in red giant stars is a rare and continuously not understood phenomenon since its discovery by Wallerstein & Sneden (1982a). Lithium being easy to observe in cool stars, many spectroscopic surveys have looked for Li-rich stars (Brown et al. 1989; Jasniewicz et al. 1999a; Charbonnel & Balachandran 2000; Monaco et al. 2011a; Lyubimkov et al. 2012; Martell & Shetrone 2013; Liu et al. 2014a; Bharat Kumar et al. 2015; Zhou et al. 2018; Smiljanic et al. 2018; De Silva et al. 2015; Gao et al. 2019; Charbonnel et al. 2020; Deepak et al. 2020; Martell et al. 2020; Magrini et al. 2021b). Depending on the adopted criteria for a star to be classified as Li-rich (see discussions in Charbonnel et al. 2020 and Chanamé et al. 2022), all surveys show that roughly one to two percent of red giant stars have enhanced photospheric lithium abundances with respect to their Li-depleted counterparts. Of the ~ 150 lithium-rich giants discovered in the last three decades, only about 20 have been observed to be super Li-rich, with an abundance of A(Li)[1] > 3.3 dex, i.e., higher than the proto-solar Li abundance. Accounting for non-local thermodynamic equilibrium (NLTE) for Li abundances, only a handful of stars have been found to have abundance of A(Li) > 4 (Martell & Shetrone 2013; Casey et al. 2016; Yan et al. 2018; Balachandran et al. 2000; Strassmeier et al. 2015; Singh et al. 2019).

Two general ideas have been explored to account for the excess amounts of lithium present in this minority of stars, namely, the production of fresh Li inside the stars themselves, or the accretion of Li-rich material from an external source. Internal Li production in red giants requires a fast transport process in the radiative layers between the hydrogen-burning shell where the unstable ^{7}Be can be produced through the pp-chains and the base of the convective envelope where Li can survive[2] (Sackmann & Boothroyd 1999; Charbonnel & Balachandran 2000; Denissenkov & Weiss 2000; Palacios et al. 2001; Denissenkov & Herwig 2004; Silva Aguirre et al. 2014; Yan et al. 2018; Casey et al. 2019; Mori et al. 2021). A number of plausible external mechanisms have also been suggested, including planetary engulfment or novae debris contaminating the outer layers of these giants (Alexander 1967; Siess & Livio 1999; Andrievsky et al. 1999; Aguilera-Gómez et al. 2016; Casey et al. 2016; Mallick et al. 2022). The occurrence and the efficiency of these different mechanisms are expected to depend on the evolution stage of the Li-rich stars, which is strongly debated, with asteroseismology potentially bringing new pieces of evidence for a handful of stars so far (Charbonnel & Balachandran 2000; Kumar et al. 2011; Yan et al. 2021; Chanamé et al. 2022).

It is within this context that we present our discovery of a unique ultra-enhanced lithium giant metal-poor Milky Way halo star, 2MASS J05241392−0336543 (hereafter referred to as J0524−0336), discovered serendipitously as part of the *R*-Process Alliance (RPA) survey. Initial high-resolution spectroscopic data collected for this star suggested a lithium abundance far greater than the Li-rich standard of A(Li) ~ 1.5. We then further collected higher S/N high resolution data

[1] A(Li)= $\log_{10}(N_{Li}/N_H) + 12$

[2] This is the so-called Cameron & Fowler (1971) process which is expected to occur in the convective envelope of Li-rich stars on the Asymptotic Giant Branch (AGB; Sackmann & Boothroyd 1992; Forestini & Charbonnel 1997).

Table 1. Properties of J0524−0336

Label	Value
2MASS star ID	2MASS J05241392−0336543
R.A. (J2000)	05:24:13.900
Decl. (J2000)	−03:37:00.300
$G_{\rm mag}$ (*Gaia* DR3)	13.343
MJD	58185.5
$v_{\rm rad}^{\rm helio}$(This work)(km s^{-1})	103.10 ± 0.80
$v_{\rm rad}^{\rm helio}$(Gaia DR3)(km s^{-1})	102.79 ± 1.35
$T_{\rm eff}$ (K)	4540 ± 140
$\log g$	1.09 ± 0.20
ξ_t (km s^{-1})	2.37 ± 0.08
[Fe/H]	-2.54 ± 0.17
$v_{\sin i}$ (km s^{-1})	11 ± 2.00
$\log(L/L_\odot)$	2.71 ± 0.10
$R\,(R_\odot)$	39 ± 15

Table 2. Photometric Temperature Calculations from Different Bands

Photometric Color	$T_{\rm eff}$ (K)	$\sigma\,T_{\rm eff}$ (K)
(B-R)	3894	64
(R-J)	4730	93
(R-H)	4687	59
(R-K)	4696	46
(B-J)	3917	49
(B-H)	3959	40
(B-K)	4014	33
(G-J)	4169	56
(G-H)	4309	41
(G-K)	4286	31
Mean	4279	51.2

for the star to confirm this enhancement, and several epochs of observations to monitor its radial velocity. The fundamental properties of J0524−0336 are listed in Table 1, with detailed description explained in the sections to follow.

This paper is outlined as follows: In Section 2, we describe our observations, data reduction, and radial velocity determinations for the candidate star. In Section 3, we thoroughly investigate the fundamental atmospheric stellar parameters, using different methods including (1D, LTE) as well as (NLTE) radiative transfer analyses, and photometric measurements to establish the stellar evolutionary status of J0524−0336. In Section 4, we present the detailed chemical abundance determinations in our star, including abundances of the light, α, and r-process elements, as well as comparison with previously discovered lithium-rich giants. In Section 5, we discuss the evolutionary status of J0524−0336 based on tailor-made stellar evolution models. Finally, we present our discussion of the results and conclusions in Sections 6 and 7, respectively.

2. OBSERVATIONS AND DATA REDUCTION

J0524−0336 was initially identified and vetted as an r-process enhanced candidate by the RPA collaboration (Hansen et al. 2018; Sakari et al. 2018; Ezzeddine et al. 2020; Holmbeck et al. 2020), from the Large Sky Area Multi-Object Fibre Spectroscopic Telescope (LAMOST) survey (Deng et al. 2012). The star was observed with the Magellan Inamori Kyocera Echelle (MIKE) spectrograph (Bernstein et al. 2003) on the Magellan-Clay Telescope at Las Campanas Observatory on three separate nights: for 1200 s on 08 March, 2018, for 7600 s, on 26 October, 2019 as well as for 120s on 03 March, 2022. All observations were taken with the 0.7" slit with the 2×2 binning setup, yielding nominal resolving powers of $R \sim 35,000$ in the red ($\lambda > 5000$ Å) and $R \sim 41,000$ in the blue, respectively.

The spectra were then reduced using the latest versions of the `Carnegie Python Distribution`[3] (Kelson 2003). Each order of each spectrum was afterwards normalized and merged into a final spectrum, covering a wavelength range of $\sim$ 3320 Å-9165 Å. For our final analysis of J0524−0336, we use the highest S/N spectrum from October 2019, with S/N$\sim$ 25 (pixel^{-1}) at 3950 Å, $\sim$ 70 at 4550 Å, $\sim$ 85 at 5200 Å, and $\sim$ 240 at 6750 Å. The final spectrum was radial-velocity, $v_{\rm rad}$, shifted by cross-correlation with the Mg I lines near 5100 Å from the spectrum of the benchmark metal-poor star HD 122563, using the spectroscopic analysis tool `Spectroscopy Made Hard` (SMH; Casey 2014). A heliocentric velocity ($v_{\rm rad}^{\rm helio}$) correction was then determined with the `rvcorrect` package in `IRAF` (Tody 1986), with $v_{\rm rad}^{\rm helio} = 103.10 \pm 0.90$ km s^{-1}. This value is in good agreement with the *Gaia* DR3 heliocentric radial velocity $v_{\rm rad}^{Gaia} = 102.79 \pm 1.35$ km s^{-1}. We also determine $v_{\rm rad}^{\rm helio} = 102.10 \pm 1.00$ km s^{-1} from the 2022 data and $v_{\rm rad}^{\rm helio} = 101.40 \pm 0.90$ km s^{-1} from the 2018 data. Based on the present data there is no evidence to support that J0524−0336 is in a binary system.

3. STELLAR PROPERTIES & FUNDAMENTAL ATMOSPHERIC PARAMETERS

Due to the significant Li enhancement of our star (see Section 4), we conduct a thorough investigation

[3] https://code.obs.carnegiescience.edu/mike

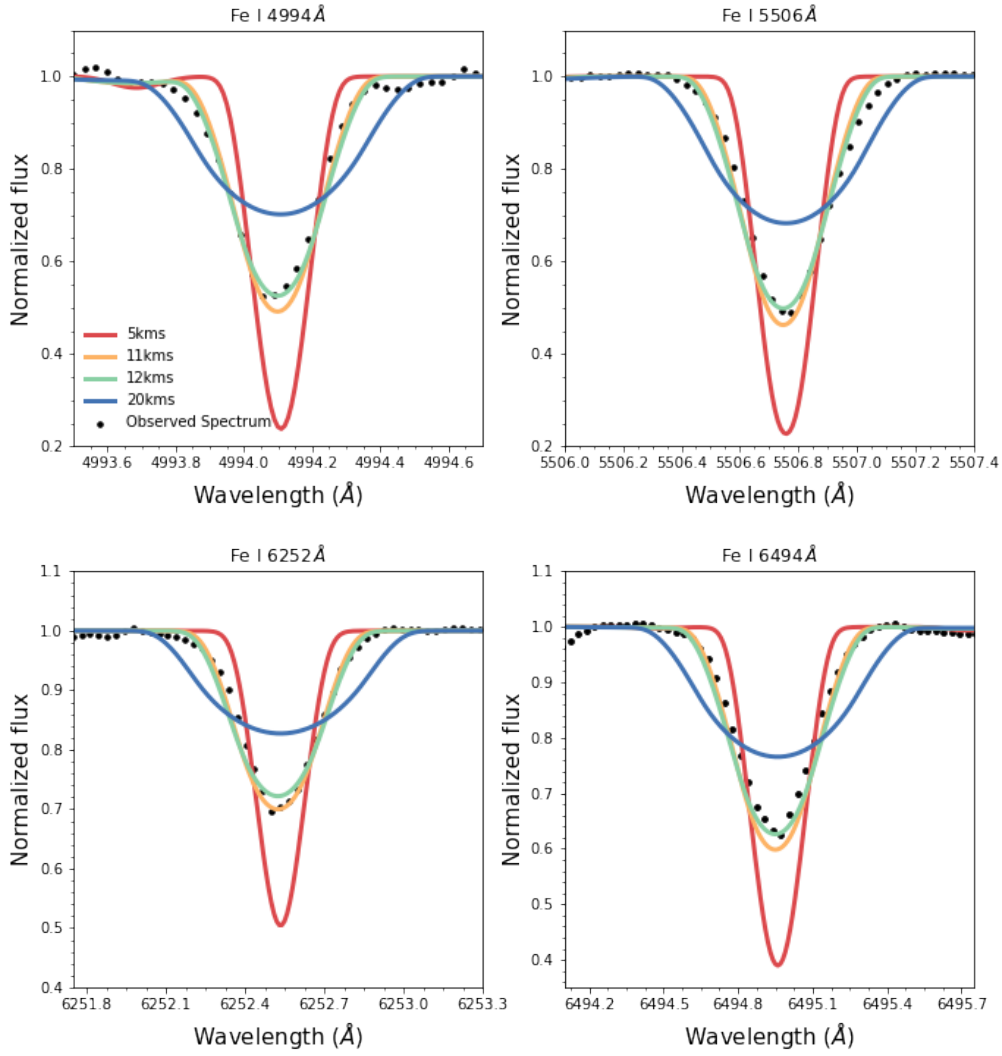

Figure 1. Synthetic spectral line profiles shown for four Fe I lines in J0524−0336, computed with different stellar projected rotational velocities $v \sin i$, ranging from 5-20 km s^{-1} (solid colored lines) shown against the observed spectra (dotted black points).

of its stellar parameters, in an attempt to accurately identify its stellar evolutionary status. We, thus, investigate the fundamental atmospheric stellar parameters (namely, the effective temperature $T_{\rm eff}$, surface gravity $\log g$, metallicity [Fe/H], and microturbulent velocity ξ_t) of J0524−0336 using spectroscopic LTE and NLTE radiative transfer models, as well as with non-spectroscopic methods implementing photometry and fundamental equations. Additionally, we investigate its stellar properties relevant to the current study, including its luminosity, radius, projected rotational velocity $v_{\sin i}$, infrared excess, and H_α emission. Below, we describe the methods and report on each of our derived properties and parameters separately.

3.1. *LTE Stellar Parameters*

We determine the fundamental atmospheric stellar parameters of J0524−0336 under the assumption of LTE using abundances of 178 Fe I and 17 Fe II lines, and employing the 2017 version of the LTE radiative transfer

code MOOG (Sneden 1973), which includes a Rayleigh scattering treatment following Sobeck et al. (2011)[4]. The Fe I and Fe II linelist was adopted from Roederer et al. (2018), with $\log gf$ values compiled from several sources (see their Table 2 and references therein). Abundances were computed using 1D, LTE, α-enhanced stellar atmospheric models from Castelli & Kurucz (2004), including standard α-element enhancement of [α/Fe] = +0.4. The abundance of Fe I and Fe II were determined using the equivalent width (EW) curve of growth method. The EW measurements were done by fitting Gaussian line profiles to the absorption lines using SMH. $T_{\rm eff}$ was determined by establishing excitation equilibrium of the Fe I abundance lines as a function of excitation potential, χ. The $\log g$ was determined by establishing an ionization equilibrium between abundances derived from the Fe I and Fe II lines. The ξ_t was estimated by requiring no trend between the abundances derived from the Fe I lines and the reduced equivalent widths ($\log(EW/\lambda)$). [Fe/H] was determined from the average of the Fe I and Fe II line abundances. The derived LTE stellar parameters are: $T_{\rm eff}$ = 4300 ± 150 K, $\log g$ = 0.02 ± 0.3, ξ_t = 3.14 ± 0.2 km s^{-1}, [Fe/H] = −2.57 ± 0.14. We estimate parameter uncertainties for $T_{\rm eff}$, $\log g$, and ξ_t assuming systematic uncertainties following the analysis in Ji et al. (2016). The [Fe/H] uncertainties were determined from the standard deviations of the Fe I and Fe II abundances.

3.2. *"Corrected" Stellar Parameters*

Systemic uncertainties can affect spectroscopic parameters estimated under the assumption of LTE. These uncertainties are larger in cool metal-poor stars, such as J0524−0336 (Bergemann & Cescutti 2010; Lind et al. 2012; Ezzeddine et al. 2017). Photometrically derived $T_{\rm eff}$ values have been demonstrated to yield smaller uncertainties than those estimated using LTE spectroscopic approaches (Casagrande et al. 2010; Frebel et al. 2013). We thus apply a "photometric correction" to the spectroscopic temperature for J0524−0336 following the method outlined in Frebel et al. (2013), tested on FGK metal-poor benchmark stars. The "corrected" temperature is hereafter referred to as $T_{\rm eff}$(FR13 corr.) and was calculated using:

$$T_{\rm eff}(\text{FR13 corr.}) = T_{\rm eff}(\text{LTE}) - 0.1 \times T_{\rm eff}(\text{LTE}) + 670,$$

which yielded $T_{\rm eff}$(FR13 corr.)= 4540 K. This value is 240 K higher than the spectroscopic LTE temperature, which agrees with the expected corrections derived in Frebel et al. (2013).

We then fixed our $T_{\rm eff}$ to $T_{\rm eff}$(FR13 corr.), and redetermined $\log g$, ξ_t, and [Fe/H] as described in Section 3.1. The "corrected" parameters are: $\log g$= 0.98 ± 0.30, ξ_t= 3.42 ± 0.20 km s^{-1}, and [Fe/H]= −2.55 ± 0.24. Increasing the $T_{\rm eff}$ to the Frebel et al. (2013) "corrected" value yielded a higher $\log g$ by 0.96 dex, as is expected.

3.3. *NLTE Stellar Parameters*

Atmospheric stellar-parameter determinations for metal-poor stars from LTE spectroscopic methods are affected by unaccounted-for departures from statistical equilibrium that can introduce significant systematic uncertainties, since line formation and populations of non-dominant species (in this case Fe I) can potentially deviate from the Saha–Boltzmann equilibrium assumed in LTE (Lind et al. 2012; Amarsi et al. 2016; Ezzeddine et al. 2017). To account for such departures, it is necessary to investigate the formation of iron lines (and thus stellar parameters) in NLTE.

Therefore, we also determine stellar parameters for J0524−0336 using 1D, NLTE radiative transfer models. The NLTE abundances were computed for Fe I and Fe II lines from their EWs using the radiative transfer code MULTI in its 2.3 version (Carlsson 1986, 1992), and employing 1D MARCS model atmospheres (Gustafsson et al. 1975, 2008) interpolated to the corresponding parameters. Blanketing from background opacities, excluding Fe lines, was employed from the MARCS opacity package (B. Plez, private communication).

The Fe I/Fe II atomic model used in the NLTE calculations is described in Ezzeddine et al. (2016, 2017). This model was built by adopting up-to-date atomic data, taking into account inelastic collisions with neutral hydrogen rates for excitation and charge-exchange processes as implemented from Barklem (2018). These collisions play an important dominant role (over electrons) in NLTE calculations of cool stars.

The NLTE stellar parameters were derived using the 1D, NLTE atmospheric stellar parameters optimization tool LOTUS[5] (Li & Ezzeddine 2022). The tool utilizes the same optimization conditions described in Section 3.1 to derive the parameters (i.e., excitation and ionization equilibrium), and employs a global curve of growth method to take into account the inter-dependence of the EW of each Fe I and Fe II line on the corresponding atmospheric stellar parameters. Additionally, error bars were constrained using a Markov Chain Monte Carlo (MCMC) algorithm. The NLTE parameters are

[4] https://github.com/alexji/moog17scat

[5] https://github.com/Li-Yangyang/LOTUS

$T_{\rm eff}$=4540 ± 144 K, $\log g$=1.09 ± 0.20, [Fe/H]=−2.54 ± 0.17 and ξ_t=2.37 ± 0.08 km s^{-1}. The $T_{\rm eff}$ and $\log g$ both agree very well with the "corrected" LTE parameters.

3.4. *Fundamental and Photometric Stellar Parameters*

In addition to spectroscopic methods, we also determine the $T_{\rm eff}$ of J0524−0336 using photometric colors. We adopt the temperature-color calibration from Casagrande et al. (2020) to determine $T_{\rm eff}$ based on photometric colors in different bands (we used 12 different colors) adopted from the 2MASS (Skrutskie et al. 2006) and *Gaia* (Gaia Collaboration et al. 2016) surveys. The derived temperatures from each color are listed in Table 2. The weighted average and statistical uncertainty is $T_{\rm eff}$= 4279 ± 51 K.

We also determine $\log g$ using a fundamental relation[6], utilizing the photometric $T_{\rm eff}$ and the *Gaia* EDR3 parallax and derived distance (Bailer-Jones et al. 2021). We adopt a mass $M = 0.8\,M_\odot$, typical of evolved giant stars at the metallicity of our star, and derive a radius of $26 \pm 2.6\,R_\odot$. We also derive a luminosity $L = 508 \pm 1.07\,L_\odot$, with $\log(L/L_\odot) = 2.71 \pm 0.10$. The bolometric correction, $BC = -0.724$, was calculated using the method outlined in Reed (1998), based on the photometric temperature and radius. The apparent visual magnitude (G = 13.348) is from *Gaia* DR3, and the distance, $d = 9065.45 \pm 1228.1$ pc was adopted from Bailer-Jones et al. (2021) derived from the *Gaia* EDR3 parallax. The extinction value, $E(B-V)$ = 0.229, is from Schlafly & Finkbeiner (2011). A fundamental $\log g$=1.22±0.26 was derived. With these parameters we redetermine ξ_t and [Fe/H] spectroscopically (using the method outlined in Section 3.1) as 3.31 ± 0.2 km s^{-1}and -2.11 ± 0.36, respectively.

Interestingly, J0524−0336 was also recently flagged as a variable star in the *Gaia* DR3, with a G magnitude variability difference between `max_mag_g_fov` and `min_mag_g_fov` of 0.153, with a median G magnitude of 13.343, and a period of 59.9 days.

3.5. *Adopted Atmospheric Fundamental Parameters*

The derived fundamental atmospheric parameters of J0524−0336 using the different methods outlined in Sections 3.1 - 3.4 are listed in Table 3. The derived NLTE $T_{\rm eff}$ and "corrected" are ∼ 300 K higher than the photometric $T_{\rm eff}$, which might be attributed to the variability of the star, as well as the significant IR-flux excess (see Section 3.7 below for details) detected in the star. The $\log g$ derived from the fundamental relation agrees well within uncertainties to those derived in NLTE and with "corrected" parameters. Therefore for our final parameters, we adopt the NLTE values for J0524−0336, $T_{\rm eff}$= 4540 ± 150 K, $\log g$= 1.09 ± 0.26, ξ_t= 2.37 ± 0.08 km s^{-1}, and [Fe/H]= −2.54±0.17 . We will use these parameters throughout the rest of the paper.

3.6. *Projected Rotational Velocity ($v_{\sin i}$)*

Rotational velocity has been linked to both external and internal lithium enhancement (Carlberg et al. 2012; Charbonnel et al. 2020). We determine the projected rotational velocity, $v_{\sin i}$, of J0524−0336 following two methods: (i) using the Full Width Half Maximum (FWHM) of several Fe I lines around 6400 Å region following the method outlined in Bruntt et al. (2010), as well as (ii) fitting the Fe I lines using synthetic spectra computed with different $v_{\sin i}$ values.

We used six isolated iron lines ranging from 6400-6500 Å (S/N ∼ 240), and corrected their FWHM for instrumental broadening using the correction values from Bruntt et al. (2010). This yielded the intrinsic total broadening of the spectrum, which is contributed by both rotation and macroturbulence. In order to solve for the rotational velocity, we first estimated our star's macroturbulence ($v_{\rm macro} = 4.96 \pm 0.45$ km s^{-1}) using the equation for luminosity class III stars from Hekker & Meléndez (2007), and implementing the stellar parameters of our star. We determine $v_{\sin i} = 10.7 \pm 1.8$ km s^{-1}. We also independently fit synthetic line spectra computed with different $v_{\sin i}$ values to several Fe I lines in the 4000-6500 Å region of J0524−0336, as shown in Figure 1. To account for possible broadening sources, we take into account microturbulent velocity broadening, radiative (Doppler) and inelastic hydrogen collisional broadening (Van der Waals), as well as instrumental broadening based on the MIKE resolution (determined by convolving a Gaussian profile with each of the Fe I lines). Based on the fits, we estimate a projected rotational velocity, $v_{\sin i} \sim 11 \pm 2$ km s^{-1}, which is consistent with our FWHM calculations following Bruntt et al. (2010). This classifies J0524−0336 as a rapidly rotating red giant metal-poor star with a projected rotational velocity > 10 km s^{-1}.

3.7. *H_α Emission & IR Excess*

Lithium enhancement in stars has been suggested to be linked to stellar properties such as infrared (IR) excess and H_α emission, as proposed in some studies such as Fekel & Watson (1998), Rebull et al. (2015), and Mallick et al. (2022). Both these properties, if observed in stars, are indicators of mass-loss events, which

[6] $\log g = 4\log T_{\rm eff} + \log(M/M_\odot) - 10.61 + 0.4\,(BC_V + m_V - 5\log(d) + 5 - 3.1\,E(B-V) - M_{\rm bol,\odot})$, where $M_{\rm bol,\odot} = 4.75$ is the solar bolometric magnitude and the constant 10.61 is calculated from the solar constants $\log(T_{\rm eff})_\odot = 3.7617$ and $\log g_\odot = 4.438$, respectively.

Table 3. Stellar Atmospheric Parameters of J0524−0336

Parameter	LTE	LTE "corrected"	NLTE	Photometric	Adopted
$T_{\rm eff}$ (K)	4300 ± 150	4540 ± 150	4540 ± 140	4279 ± 305	4540 ± 140
$\log g$	0.02 ± 0.30	0.98 ± 0.30	1.09 ± 0.20	0.8 ± 0.24	1.09 ± 0.20
ξ_t (km s^{-1})	3.14 ± 0.20	3.42 ± 0.20	2.37 ± 0.08	2.92 ± 0.09	2.37 ± 0.08
[Fe/H]	-2.57 ± 0.14	-2.55 ± 0.24	-2.54 ± 0.17	-2.52 ± 0.18	-2.54 ± 0.17

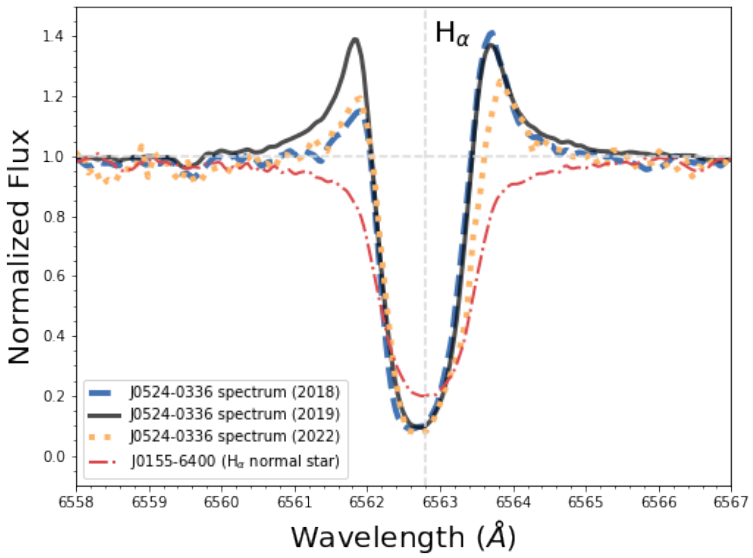

Figure 2. H_α line profile observed at different epochs in 2018, 2019 and 2022, respectively, in J0524−0336. Also shown, for comparison, is the H_α profile for the H_α-normal metal-poor star J0155−6400 with similar stellar parameters as J0524−0336.

have been connected to multiple channels of lithium enhancement (de la Reza et al. 1996; de la Reza et al. 1997). We therefore investigate both IR excess and H_α in J0524−0336. Figure 2 shows the H_α line profile in J0524−0336, observed at three different epochs, in 2018, 2019, and 2022, respectively. Also shown, for comparison, is the H_α profile for the metal-poor star, J0155−6400, with similar stellar parameters as J0524−0336 and no Li detection. We observe emission in the H_α wings in all observation epochs of J0524−0336 resembling a P-Cygni profile. Interestingly, however, each of these emission profiles are different for each epoch, signifying strong and variable activity, possibly due to mass-loss events or the presence of a circumstellar disk around the star. Additionally, we note the assymetric nature of the emission around the wings, signifying possible outflows. Consequently, we also looked into the infrared photometry for J0524−0336 from the WISE[7] all-sky data colors (Wright et al. 2010). The IR- excess or enhancement in stars typically has WISE bands difference of $W1 - W4 > 0.5$ (Yan et al. 2018). Interestingly, WISE reports $W1 - W4 = 1.63 \pm 0.02$ for J0524−0336, indicating a clear and strong IR excess, which further points to stellar activity and possible mass-loss events in J0524−0336. IR excesses have been detected in 1% of all giant stars, as compared to the 7% lithium-enhanced giant stars discovered in the Milky Way (Rebull et al. 2015; Martell et al. 2020). No clear connection has yet been made between IR excess and Li-rich stars, however, non-traditional mixing mechanisms enhancing photospheric Li abundances (such as rotation-driven mixing) might need to be invoked to explain this phenomenon.

4. CHEMICAL ABUNDANCES

[7] https://wise2.ipac.caltech.edu/docs/release/allsky/

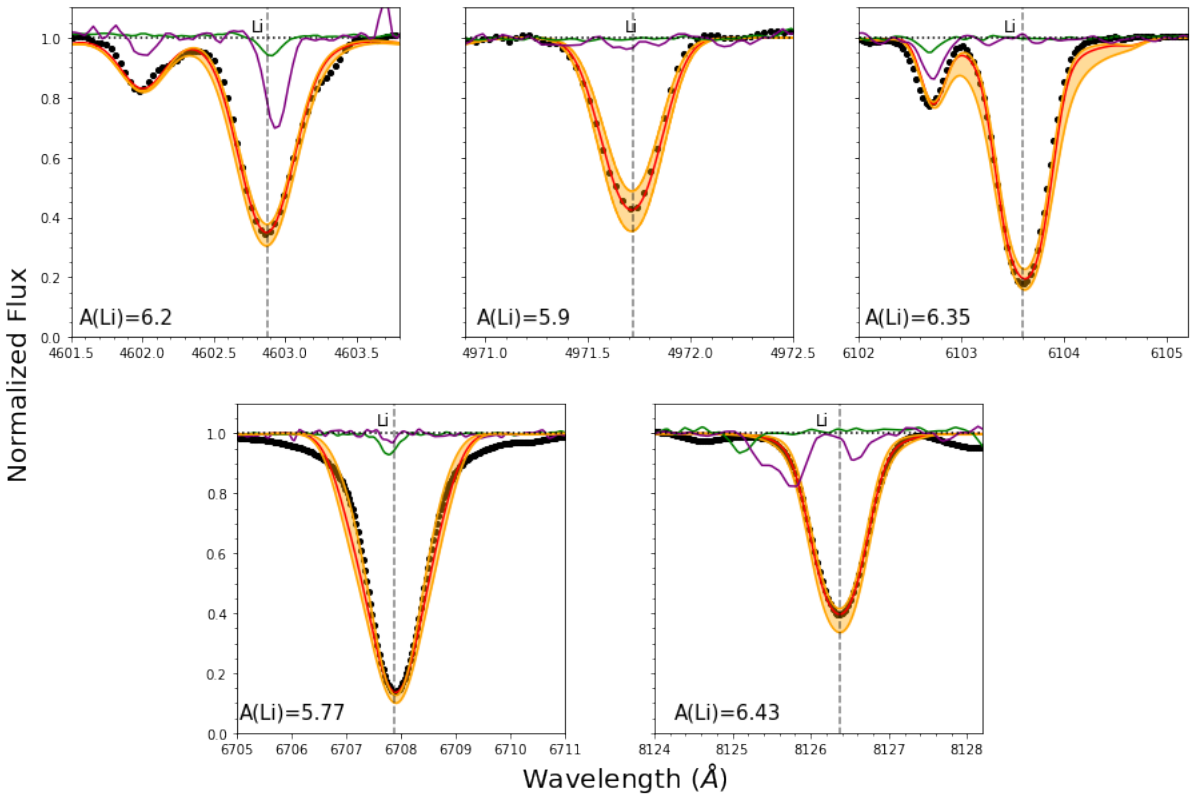

Figure 3. Line profiles, as well as synthetic spectral fits, for the 5 strong lithium lines detected in J0524−0336. The $\pm\sigma = 0.25$ abundance fits are also shown in the shaded orange. For comparison, we also display the same Li lines for the two metal-poor stars at similar [Fe/H] as J0524−0336, HE 0048−1109 (purple) with A(Li)= 2.34, and HE 0324−0122 (green) with A(Li)= 0.78.

We derive abundance measurements, as well as upper limit estimates for the light, α, and Fe-peak elements for J0524−0336 using the same radiative transfer models and spectroscopic tools described in Section 3. We computed the abundance ratios relative to H and Fe, adopting the solar photospheric abundances from Asplund et al. (2009). The abundances were derived using line-by-line EW and COG analysis, except for Li, C, O, Al, and the neutron-capture elements, where spectral profile synthesis were fit to each line. The linelist was adopted from Roederer et al. (2018) (see their Table 2 for atomic data references) for lines which could be detected in J0524−0336. Isotopic ratios were included for Li, C (see below for details), as well as for several neutron-capture elements from Sneden et al. (2008)[8] and Placco et al. (2021). Hyper-fine structure (HFS) was considered for the Fe-peak elements, including Sc, V, Mn, and Co, when necessary. Upper limits were determined by matching the noise levels in the observed spectral lines with the corresponding synthetic spectral lines. Upon examining abundances from multiple lines for each element, outlying abundances were removed and an the average abundance and standard deviation was recorded for each element. For elements with only 2-5 lines measured, we estimated standard deviations by multiplying the range of values covered by our line abundances with the k-factor following Keeping (1962). For elements with one line only, we adopt an uncertainty between 0.1 and 0.3 dex, depending on the data and fit quality. The abundance averages and the corresponding standard deviations are reported in Table 4. The line-by-line abundances of each of these elements is recorded in Table 6. We record systematic uncertainties in our chemical abundances resulting from uncertainties in the model atmospheric parameters, by varying the stellar parameters by typical uncertainties in the positive direction (i.e., $\Delta T_{\rm eff}$= +150 K, $\Delta \log g$= +0.30 dex, Δ[Fe/H] = +0.30 dex, and $\Delta\xi_t$=0.2 km s^{-1}), and recording the change in abundance. This is shown in Table 5. All changes are within expected error bars.

[8] https://github.com/vmplacco/linemake

4.1. *Lithium Abundance in J0524−0336*

Lithium abundance was derived from synthesizing the Li lines at 4602 Å, 4971 Å, 6103 Å, 6707 Å and 8126 Å. An isotopic ratio of ^{6}Li/^{7}Li = 0.005 was adopted. As

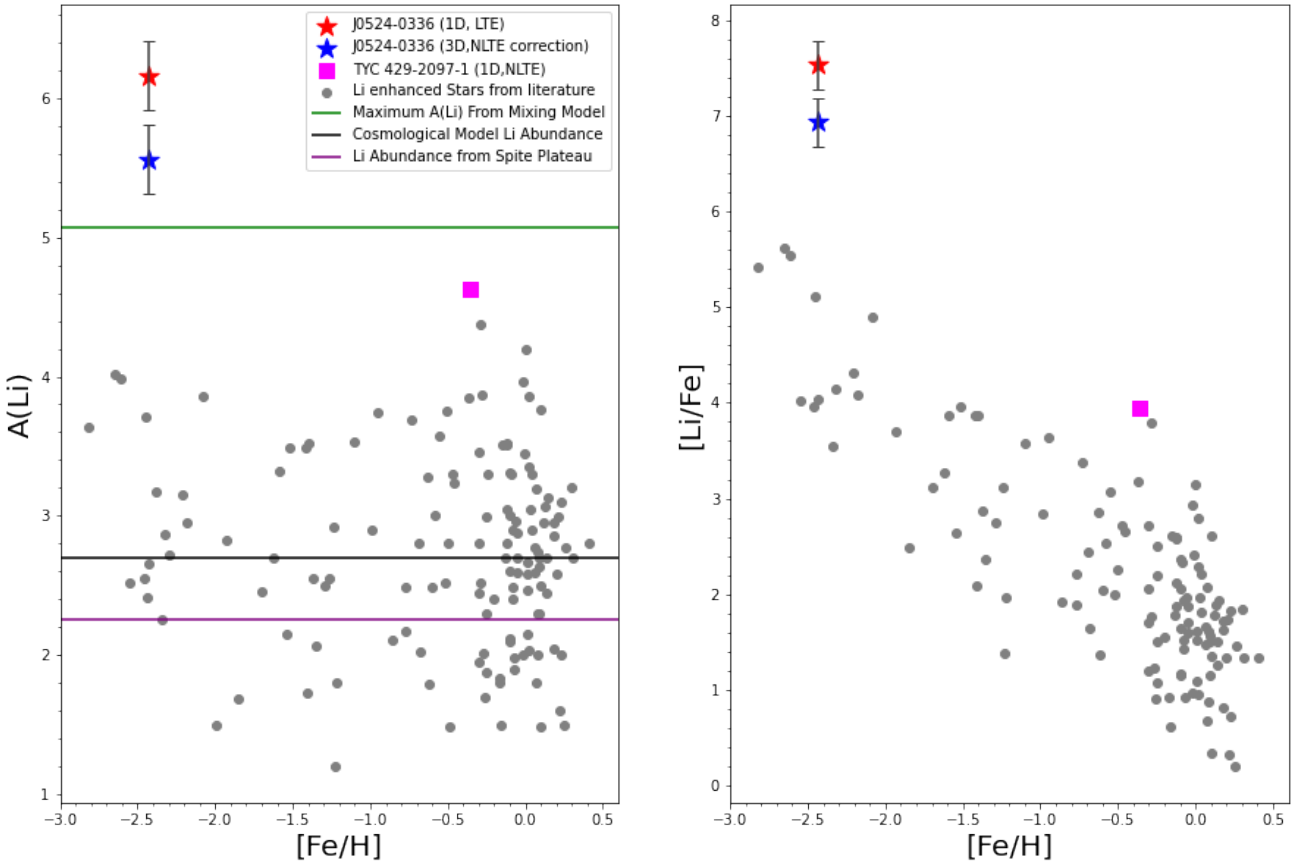

Figure 4. Absolute lithium abundance, A(Li), (left panel) and [Li/Fe] (right panel) for J0524−0336 (derived using 1D, LTE and 3D, NLTE corrected values in red and blue stars, respectively) plots versus [Fe/H], and other lithium-rich giant stars from the literature. The star with the next highest Li abundance after J0524−0336, TYC 429-2097-1 (Yan et al. 2018), is also shown on the plots by the magenta square. The primordial cosmological Li abundance (black line), the Spite Plateau (magenta line) as well as the maximum Li enhancement from mixing models (green line) from Yan et al. (2018) are also shown. References from: Luck 1982; Wallerstein & Sneden 1982b; Hanni 1984; BRO 1989; Gratton & D'Antona 1989; McWilliam & Rich 1994; Carney et al. 1998; Jasniewicz et al. 1999b; Smith et al. 1999; Hill & Pasquini 1999; Balachandran et al. 2000; Reyniers & Van Winckel 2001; Drake et al. 2002; Canto Martins et al. 2006; Lèbre et al. 2009; Gonzalez et al. 2009; Carlberg et al. 2010; Alcalá et al. 2011; Andrievsky et al. 1999; Kumar et al. 2011; Ruchti et al. 2011; Monaco et al. 2011b; Kirby et al. 2012; Anthony-Twarog et al. 2013; Martell & Shetrone 2013; Adamów et al. 2014; Liu et al. 2014b; Monaco et al. 2014; Adamów et al. 2015; Carlberg et al. 2015; D'Orazi et al. 2015; Jofré et al. 2015; Kirby et al. 2016; Casey et al. 2016; Yan et al. 2018.

can be seen in Figure 3, all the Li lines in this star are strikingly strong, with the line at 6707 Å being especially prominent. Li was also detected in the lines at 4273 Å and 4132 Å, however, as they were blended they were not used in the final abundance average. The five remaining lines yielded lithium abundances of A(4602Å)=6.20, A(4973Å)=5.90, A(6103Å)=6.35, A(6707Å)=5.77, A(8126Å)=6.43, respectively. We thus report an average Li abundance for J0524−0336 of A(Li)(1D, LTE)= 6.13 ± 0.25, and a ratio relative to Fe of [Li/Fe]=+7.53. We note that the 6707 Å resonance line, however, yields a lower Li abundance than the rest of the lines (up to 0.5 dex). This dispersion can be attributed to the asymmetric nature of this particular line and the strength of its wings. Wang et al. (2021) investigated this (and other) Li line in details using a 3D, NLTE analysis. They indicate that as the A(Li) increases, the line formation pushes toward higher layers in the stellar photosphere with significantly lower temperatures that deeper layers which can drive the models away from hydrostatic equilibrium. Therefore, a full 3D hydrodynamic simulation is needed to accurately fit the 6707 Å line. Such an endeavor is, however, beyond the capability and the scope of this paper. By excluding the 6707 Å line from the Li average of J0524−0336 yields a higher abundance of A(Li)=6.22 and [Li/Fe]=+7.60.

The observations and corresponding synthesis of the lines are shown in Figure 3. For comparison, we also show in this figure the same Li lines for two other Li-normal metal-poor stars with similar stellar parameters

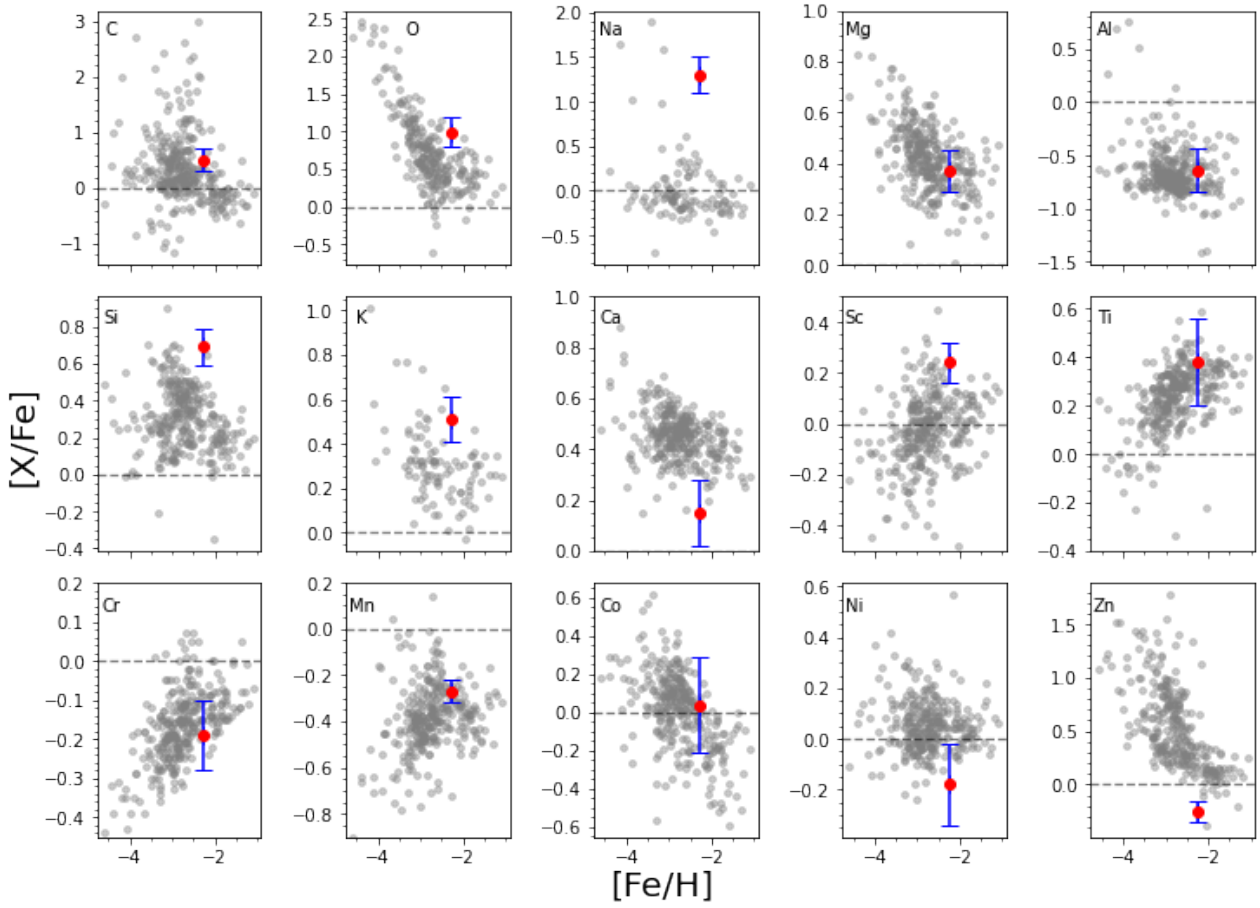

Figure 5. The [X/Fe] abundance ratios of C through Zn in J0524−0336 , compared to Milky Way halo stars from Yong et al. (2013) and Roederer et al. (2014).

as J0524−0336. The mere presence of seven detectable lithium lines is highly unusual in such a metal-poor star, as it is more common that only the line at 6707 Å can sometimes be detected, even in Li-rich giants. We compare the Li abundance in J0524−0336 to other Li-rich star in the literature, as shown in Figure 4. To the best of our knowledge, both A(Li) and [Li/Fe] in J0524−0336 are significantly higher than any other Li-rich star reported in the literature to date. It can be seen in Figure 4 that the next highest lithium-enhanced giant, TYC 429-2097-1 (Yan et al. 2018), has A(Li)(LTE)=4.63 and is at a much higher metallicity ([Fe/H]=−0.36) than our star. Thus, J0524−0336 is the first star ever discovered to have an a lithium abundance of A(Li)> 5 and [Li/Fe]> +6 at such a low metallicity. This significant enhancement relative to other Li-rich Milky Way stars suggests a novel or different method of lithium accretion or production within J0524−0336, or a similar process occurring on extremely short timescales. NLTE effects can be strong for metal-poor giant stars, and particularly the Li resonance line at 6707 Å has been shown to be prone to both 3D and NLTE effects if strong, as is the case in Li-rich stars (Lind et al. 2013; Wang et al. 2021). We thus apply a 3D, NLTE abundance correction using Wang et al. (2021)'s pre-computed 3D, NLTE Li abundance grid, and estimated with their publicly available interpolation tool `Breidablik`[9]. We derive a 3D, NLTE-corrected abundance correction for J0524−0336 of Δ(Li)=A(3D, NLTE)- A(1D, LTE) = −0.6 dex by interpolating to its corresponding adopted metallicity and stellar parameters, which renders the Li abundance in J0524−0336 A(Li)(3D, NLTE)=5.62 and [Li/Fe](3D, NLTE)=+7.00 (we adopt a solar lithium abundance $A(Li)_{\odot}$=1.05; Asplund et al. 2009). Interestingly, despite these corrections, J0524−0336 retains its status as the star with the highest Li detected to date, and is significantly higher than other Li-rich stars (see Figure 4).

4.1.1. *Carbon and Oxygen*

[9] https://github.com/ellawang44/Breidablik

Table 4. Element Abundances in J0524−0336

El.	N	$\log\epsilon$ (X)$_\odot$	$\log\epsilon$(X)	[X/H]	[X/Fe]	σ[X/H]
Li(1D,LTE)	4	1.05	6.22	+5.17	+7.60	0.25
Li(3D,NLTE)	4	1.05	5.62	+4.57	+7.00	0.25
CH	1	8.43	5.70	−2.73	−0.13	0.20
CH(corr.)[a]	1	8.43	6.34	−2.09	+0.51	0.20
O I	1	8.69	7.41	−1.28	+0.99	0.20
Na I(1D,LTE)	1	6.24	5.26	−0.98	+1.30	0.20
Na I(1D,NLTE)	1	6.24	5.06	−1.18	+1.10	0.20
Mg I(1D,LTE)	7	7.60	5.70	−1.90	+0.37	0.19
Mg I(1D,NLTE)	7	7.60	5.75	−1.85	+0.42	0.19
Al I(1D,LTE)	1	6.45	3.53	−2.92	−0.64	0.20
Al I(1D,NLTE)	1	6.45	4.03	−2.42	−0.14	0.20
Si I	2	7.51	5.93	−1.58	+0.69	0.17
K I(1D,LTE)	2	5.03	3.27	−1.76	+0.51	0.06
K I(1D,NLTE)	2	5.03	2.57	−2.46	−0.21	0.06
Ca I(1D,LTE)	21	6.34	4.21	−2.13	+0.15	0.21
Ca I(1D,NLTE)	21	6.34	4.31	−2.03	+0.25	0.21
Sc II	11	3.15	1.11	−2.04	+0.24	0.28
Ti II	43	4.95	3.05	−1.90	+0.38	0.35
Cr I	16	5.64	3.18	−2.46	−0.19	0.17
Mn I	4	5.43	2.88	−2.55	−0.27	0.37
Fe I	178	7.50	5.24	−2.26	+0.01	0.36
Fe II	17	7.50	5.11	−2.39	−0.12	0.15
Co I	3	4.99	2.75	−2.24	+0.04	0.10
Ni I	16	6.22	3.77	−2.45	−0.18	0.30
Zn I	2	4.56	2.03	−2.53	−0.25	0.03
Sr	2	2.87	0.42	−2.45	+0.10	0.29
Y	15	2.21	−0.19	−2.40	+0.14	0.08
Zr	12	2.58	0.46	−2.12	+0.43	0.20
Nb	1	1.46	<0.18	<-1.28	$<+1.27$	0.30
Mo	1	1.88	<-0.17	<-2.05	$<+0.50$	0.30
Ru	1	1.75	<0.30	<-1.45	$<+1.10$	0.30
Rh	1	0.91	<0.56	<-0.35	$<+2.20$	0.20
Pd	1	1.57	<0.67	<-0.90	$<+1.66$	0.30
Ag	1	0.94	<0.04	<-0.90	$<+1.65$	0.30
Ba	5	2.18	0.08	−2.10	+0.47	0.10
La	19	1.10	−0.64	−1.74	+0.81	0.12
Ce	12	1.58	−0.48	−2.06	+0.49	0.09
Pr	9	0.72	−0.74	−1.46	+1.09	0.08
Nd	26	1.42	−0.32	−1.74	+0.81	0.13
Sm	10	0.96	−0.48	−1.44	+1.13	0.09
Eu	12	0.52	−0.69	−1.21	+1.34	0.10
Gd	7	1.07	−0.42	−1.49	+1.07	0.09
Dy	12	1.10	−0.28	-1.38	+1.18	0.11
Ho	1	0.48	<-0.85	<-1.33	$<+0.92$	0.3
Er	7	0.92	−0.49	-1.41	+1.16	0.36
Tm	2	0.10	−1.15	-1.25	+1.30	0.14
Lu	1	0.10	<-1.05	<-1.15	$<+1.40$	0.10
Hf	3	0.85	−0.73	−1.58	+0.99	0.06
Ir	1	1.38	<0.03	<-1.35	$<+1.22$	0.30
Pb	1	1.75	<-0.20	<-1.95	$<+0.62$	0.30
Th	2	0.02	−1.28	−1.30	+1.27	0.21
U	1	−0.54	<-0.99	<-0.45	$<+2.12$	0.20

[a] Following Placco et al. (2014).

We derive O abundance from the forbidden [O I] line at 6300 Å. While this line is commonly found to be weak, and often blended with a telluric feature in metal-poor stars, we find a very good fit and derive [O/Fe]=0.99. We derive the C abundance in J0524−0336 by fitting the CH G-band at 4313 Å. We estimate a carbon abundance of A(C)=5.7 and a ratio relative to metallicity of [C/Fe]=−0.13. As can be seen in Figure 5, this is not unusual compared to other low-metallicity halo stars from Yong et al. (2013) and Roederer et al. (2014). We were unable to fit the weak NH band between 3355–3365 Å, and thus could not estimate an N abundance.

The $^{12}C/^{13}C$ isotopic ratio is a strong indicator of the extent of mixing processes in the red giant branch (RGB) stage of stellar evolution (Charbonnel et al. 1998; Charbonnel & Zahn 2007). To derive this ratio, we fix the carbon abundance derived from the 4313 Å feature to A(C)=5.7, and derive $^{12}C/^{13}C = 10 \pm 3$ from the 4217 Å line. This value suggests substantial processing of ^{12}C into ^{13}C in J0524−0336. Carbon is usually depleted throughout the lives of giant stars. We thus determine and correct for the evolutionary depletion of C due to processing in J0524−0336. We determine a correction of 0.64 dex using the online tool[10] described in Placco et al. (2014). This renders a final [C/Fe]=+0.51, which classifies J0524−0336 slightly below being a Carbon Enhanced Metal-Poor (CEMP) star ([C/Fe] > 0.7).

4.1.2. *Light Elements*

In addition to Li, C, and O, we also derive light ($Z < 30$) element abundances of Na, Mg, Al, Si, K, Ca, Sc, Ti, Cr, Mn, Co, Ni, and Zn for J0524−0336 , following our abundance analysis of light elements described in Ezzeddine et al. (2020). The derived abundances are listed in Table 4, and are compared to other MW field stars from Yong et al. (2013) and Roederer et al. (2014) in Figure 5.

As already mentioned above, NLTE corrections can be important for non-dominant species in the atmospheres of metal-poor giant stars. We thus investigate NLTE corrections for several elements, when available from the `INSPECT`[11] database (Lind et al. 2011). We determine an average NLTE correction for Na I of −0.2 dex from the seven Na I lines we detected in J0524−0336. We derive a −0.7 dex NLTE correction for K I line at 7698 Å from Takeda et al. (2002). Similarly, we interpolate NLTE corrections for our Mg I abundance from Osorio et al. (2015), and we find a negligible average correction of < 0.05 dex for J0524−0336. For Al I, we determine the abundance from the 3961 Å line, which is heavily affected by NLTE in cool metal-poor stars (Nordlander & Lind 2017). We estimate a NLTE correction of ∼ 0.5 dex based on their published grids and the stellar parameters of J0524−0336. Finally, we estimate a ∼ 0.1 dex NLTE correction for Ca I from Mashonkina et al. (2016). For the consistency of comparisons with literature abundances, derived in LTE, we only show our LTE abundances of J0524−0336 in Figure 5, however, we list both LTE and NLTE values whenever relevant in Table 4.

The abundances of all light elements ($Z < 30$) in J0524−0336 agree with the trends typically observed in metal-poor MW halo stars, except for Na, which seems to be enhanced related to the MW, with [Na/Fe](1D, LTE)= +1.30. Additionally, both Ni and Zn seem to be low as compared to the MW field stars. We note that no connection between the peculiarity of the abundances of these elements and the Li enhancement has, however, been established. Our element abundance derivations also agree well with those derived for J0524−0336 in Ezzeddine et al. (2020).

4.2. *Neutron-Capture Element Abundances*

We also measure abundances of neutron-capture elements in our star. J0524−0336 was originally identified and classified as a highly enhanced r-II star ([Eu/Fe]> +0.7; Holmbeck et al. 2020) in Ezzeddine et al. (2020), from measurements of Sr, Ba, and Eu abundances. We re-derived abundances of these elements, in addition of other neutron-capture elements from our high-resolution, high-S/N spectrum. The Eu abundance was derived from 12 Eu II lines, which rendered A(Eu)= −0.69±0.10 and [Eu/Fe]=+1.34±0.10. This agrees with the value derived in Ezzeddine et al. (2020). We also derive [Ba/Fe]=+0.47 ± 0.10, with [Ba/Eu]= −0.87 ± 0.20, suggesting a major contribution of neutron-capture elements in J0524−0336 from an *r*-process origin. It is worth noting that this *r*-process enhancement is unlikely to be related to the Li enhancement in J0524−0336.

In addition to Eu and Ba, we measure abundances for Sr, Y, Zr, La, Ce, Pr, Nd, Sm, Gd, Dy, Er, Tm, Hf, and Th, as well as upper limits for Nb, Mo, Ru, Rh, Pd, Ag, Tb, Lu, Ir, Pb, and U. Figure 6 shows the neutron-capture abundance pattern for J0524−0336 with the scaled solar *r*-process pattern relative to Eu and the scaled *s*-process pattern relative to Ba from Sneden et al. (2008). The abundance patterns of J0524−0336 closely matches that of the scaled *r*-process, except for Sr and Y from the first *r*-process peak.

5. STELLAR EVOLUTIONARY STATUS OF J0524−0336

[10] http://vplacco.pythonanywhere.com/
[11] http://www.inspect-stars.com/

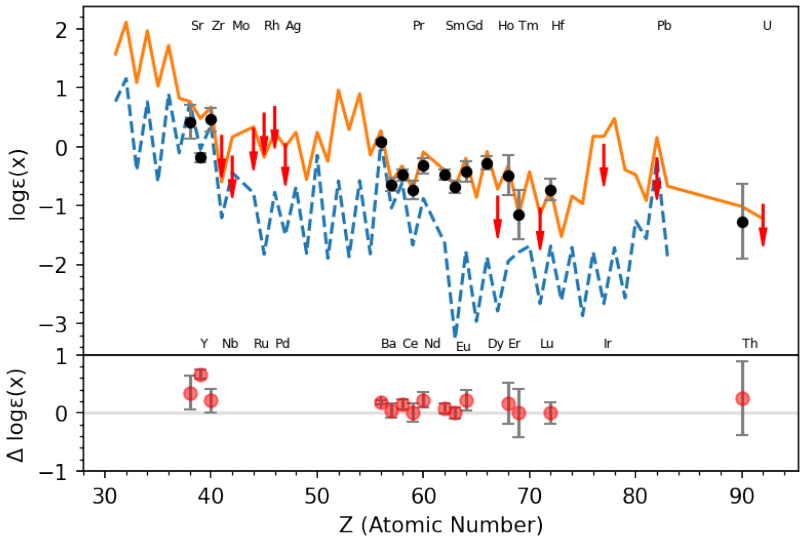

Figure 6. Derived neutron-capture abundances (black circles), as well as upper limits (red downward arrows) in J0524−0336 overplotted against the scaled solar *r*-process (orange solid line) and *s*-process (blue dashed line) abundance patterns from Sneden et al. (2008). The lower panel shows the residual plot for the abundances we measured with respect to the solar *r*-process pattern.

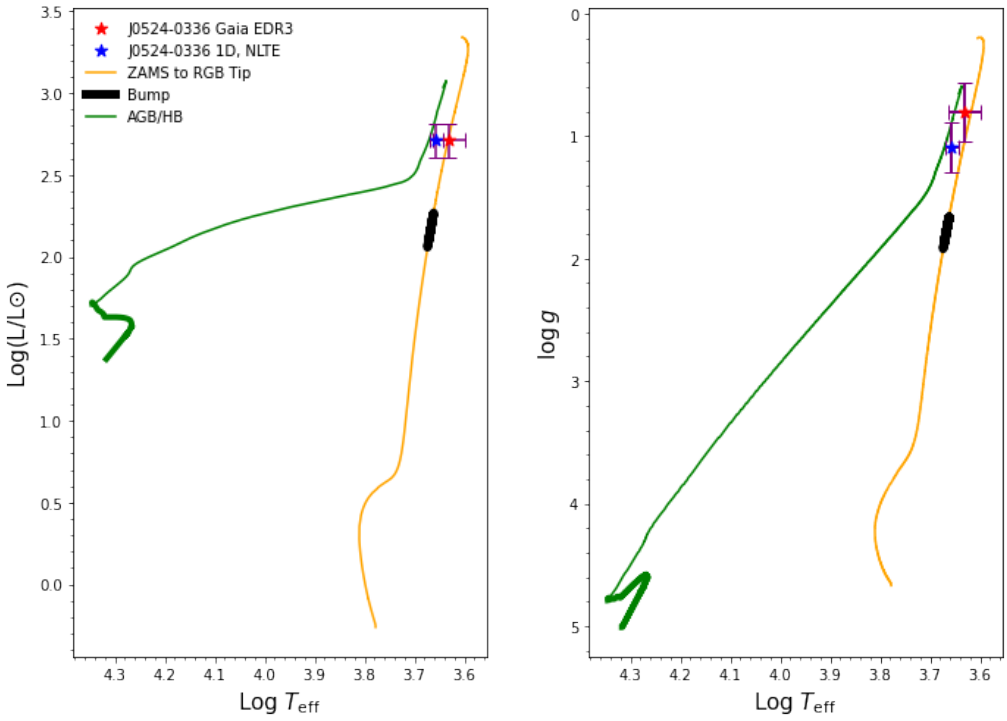

Figure 7. J0524−0336 overplotted on the stellar evolutionary track in the HRD and the Kiel diagram (left and right panels, respectively) of a 0.8 $M_\odot$ model computed with the initial [Fe/H], [C/Fe], [O/Fe], and [Na/Fe] of J0524−0336. Both *Gaia* DR3 and 1D, NLTE stellar parameters are shown for comparison. Different stellar evolutionary phases are highlighted on each diagram. The orange line goes from the zero age main sequence up to the RGB tip, and the green one from the zero age horizontal branch to the occurrence of the first thermal pulse on the AGB. The RGB bump (black bold), and the location where central He-burning occurs on the horizontal branch (bold green) are also shown on the plots.

To understand the ultra Li enhancement in J0524−0336 (A(Li)> 5), it is crucial to establish its evolutionary status. We compute tailored stellar evolution mod-

Table 5. Abundance uncertainties due to fundamental atmospheric stellar parameter uncertainties.

El.	$\Delta\ T_{\rm eff}$ ($\pm\sigma$)	$\Delta\ \log g$ ($\pm\sigma$)	$\Delta\ \xi_t$ ($\pm\sigma$)	Δ[Fe/H] ($\pm\sigma$)
Li	±0.33	±0.10	±0.01	±0.10
O I	±0.09	±0.03	±0.01	±0.03
Mg I	±0.15	±0.07	±0.03	±0.02
Al I	±0.21	±0.12	±0.03	±0.07
Si I	±0.11	±0.05	±0.02	±0.03
K I	±0.14	±0.03	±0.02	±0.01
Ca I	±0.12	±0.03	±0.01	±0.02
Sc II	±0.03	±0.05	±0.03	±0.01
Ti II	±0.02	±0.03	±0.03	±0.01
Cr I	±0.21	±0.05	±0.03	±0.03
Mn I	±0.22	±0.06	±0.02	±0.04
Fe I	±0.19	±0.05	±0.03	±0.03
Fe II	±0.04	±0.06	±0.02	±0.02
Co I	±0.22	±0.09	±0.05	±0.09
Ni I	±0.15	±0.04	±0.01	±0.02
Zn I	±0.03	±0.03	±0.00	±0.01

els using the latest version of the stellar evolution code STAREVOL (see Dumont et al. 2021b for references and details on the equation of state, opacities, and nuclear reactions). The initial chemical composition accounts for the values of [Fe/H], [C/Fe], [O/Fe], and [Na/Fe] derived in this work (see Section 4 and Table 4 for values). We use a gray atmosphere and define the stellar effective temperature and radius at the optical depth $\tau = 2/3$. The mass-loss rate follows Reimers (1975) empirical relation (with $\eta_R = 0.5$) from the zero-age main sequence up to central He exhaustion and switches to Vassiliadis & Wood (1993)'s prescription on the asymptotic giant branch (AGB). We adopt a mixing length parameter $\alpha_{\rm MLT} = 1.5$, and we assume the Schwarzschild criteria for convective stability. We include the effects of the thermohaline instability as described in Charbonnel & Zahn (2007) and Lagarde et al. (2012). We also compute models with thermohaline mixing and solid-body rotation, to predict the evolution of the surface stellar rotation rate under conservative assumptions for such a low-mass star.

The position of J0524−0336 on the HR diagram and on the Kiel diagram is well fit by the evolutionary track of a model with initial mass of 0.8 $M_\odot$ (see Figure 7). Given the uncertainties on the stellar parameters, J0524−0336 appears to be located either on RGB above the predicted location of the bump, or on the e-AGB before the occurrence of the thermal pulses on the AGB (TP-AGB). It has a much cooler temperature than the position of the horizontal branch (HB), which is the metal-poor counterpart of the red clump (RC) for metal-rich giants. Although no asteroseismic constraint is available for J0524−0336, we can safely conclude that it is currently *not* undergoing central He-burning. We checked the values of different global asteroseismic quantities computed with the same prescriptions as in Lagarde et al. (2012) in our model at the two evolution points on the RGB and early-AGB at the luminosity of J0524−0336 (both have an effective temperature compatible with the derived values within the error bars), and found no significant differences. In particular, the predicted asymptotic period spacing between adjacent l=1 modes at these two points are lower than that predicted by our model on the HB (36.6 and 27.2 s respectively on the RGB and on the early-AGB, to compare to $\sim$ 316 s at the end of central He-burning on the HB).

Within the error bars on the luminosity and effective temperature of J0524−0336, both on the RGB and the e-AGB, the model predicts a value of 9.6 for the $^{12}C/^{13}C$ ratio (to compare to the value of 42 obtained after the first dredge-up), due to the effect of the thermohaline mixing that is predicted to occur at the RGB bump. This is in very good agreement with the value we derived of $^{12}C/^{13}C$=10, confirming that J0524−0336 has already undergone thermohaline mixing when it has previously crossed the RGB bump. The predicted rotation rate is 1.2 km s^{-1}, in agreement with the values for stars at this evolution stage and metallicity (Cortés et al. 2009), but much lower than that derived in this study (see Section 3.6).

6. DISCUSSION

The evolutionary status of Li-rich giants has long been debated. Charbonnel & Balachandran (2000) found an accumulation of such stars around the RGB bump and on the e-AGB, this later phase being in agreement with our conclusions for J0524−0336 . Interestingly, the next most highly enhanced lithium star (A(Li)=4.51) is probably located at the RGB bump (Yan et al. 2018). Others studies, sometimes using additional constraints based on asteroseismology parameters, concluded that a large fraction of enhanced lithium giants are actually red clump (RC) stars presently burning He in their central convective core, the rest being either close to the RGB bump or randomly distributed along the advanced phases (Kumar et al. 2011; Silva Aguirre et al. 2014; Casey et al. 2019; Yan et al. 2020; Kumar & Reddy 2020; Martell et al. 2021; Yan et al. 2021). The predominence of Li-rich RC stars was however challenged by Chanamé et al. (2022) who modeled the expected masses and Li properties of a field population of RC stars such as that observed by the GALAH survey and

by *Kepler*, and found that the distribution of Li in RC stars is actually consistent with standard model predictions. As of today, there is thus no clear consensus, and different paths to Li-enrichment remain to be explored.

Several mechanisms have been suggested in the literature to try to explain Li-richness in giant stars. These can be broadly divided into external and internal mechanisms. External mechanisms include the presence or interaction with a stellar or sub-stellar companion (such as planetary engulfment or binary interactions), while internal mechanisms include non-traditional or enhanced mixing processes. In what follows, we discuss some of these different mechanisms, linking them to the observable properties of J0524−0336, to try to explain its extreme lithium enhancement relative to other stars in the Milky Way.

6.1. *External Enrichment*

6.1.1. *Planetary Engulfment*

One mechanism that has been proposed for lithium enhancement in giant stars is planetary engulfment (Siess & Livio 1999). Planets below a certain mass threshold can dissolve in the convective envelope of a host star, which can (in some cases) lead to lithium (as well as other elemental) enhancement, and is postulated to be observed in the photospheric abundances of giant stars with $1.5 \leq \mathrm{A(Li)} \leq 2.2$. Aguilera-Gómez et al. (2016) have attempted to model lithium enrichment via the engulfment of a planet or a brown dwarf across a range of stellar metallicities and sub-stellar component masses, where they showed that planetary engulfment is unable to account for giant stars with $\mathrm{A(Li)} \geq 2.2$. This has been further confirmed by follow-up studies studies by Aguilera-Gómez et al. (2020). It is unlikely that a star at such a low metallicity as J0524−0336 would be able to form a planet, however, as an academic exercise, we nevertheless attempt to derive the substellar component parameters (including the mass and initial Li abundance) that would be theoretically required to account for the Li abundance in J0524−0336. We adopt the equations in Carlberg et al. (2012) (see their Appendix), starting with a star of similar mass to J0524−0336 ($0.8\,\mathrm{M}_{\odot}$) to estimate the Li abundance the star would have after the substellar component engulfment event. We adopt a ratio of the mass of the planet to the mass of the stellar envelope of 0.19, with the mass of the envelope being 0.05 the mass of the star. We show the results in Figure 8. The left panel shows the "Final" expected Li abundance of the star, starting with an "initial" Li abundance of A(Li)=2.2, after engulfing a planet with different intrinsic Li abundances, ranging from A_p(Li)=3.3 to 7.5, as a function of planet mass (in Jupiter masses, M_J). The right panel of Figure 8 shows the same thing, however, starting from a highly enriched "intrinsic" stellar Li abundance of A(Li)=4.0, for example, a star that has been previously enriched by an internal-mixing process. According to the the models outlined in Carlberg et al. (2012), regardless of the "initial" stellar Li abundances (A(Li)=2.2 and A(Li)=4.0), the "final" stellar photospheric Li abundances are expected to increase as a function of planet mass and intrinsic planetary Li content. For both cases, however, an unrealistically high intrinsic planetary Li content (A_p(Li)>7.0) is needed to reproduce the Li abundance in J0524−0336. Additionally, it would take a large planet ($\geq 10\,\mathrm{M}_J$) to account for this level of Li enrichment in J0524−0336. Both scenarios seem unlikely, given our current understanding of intrinsic planetary lithium content. Additionally, it has also been postulated that planets are unlikely to form around FGK stars with metallicities below [Fe/H]< -2.0 (Fischer & Valenti 2005). We can thus dismiss planetary engulfment as a primary mechanism of Li enrichment in J0524−0336.

6.1.2. *Interaction with a Binary Stellar Companion*

The presence and interaction with a binary companion has been proposed as a scenario to explain lithium enhancement in stars. For example, Casey et al. (2019) proposed that tidal interactions from a companion star could create internal mixing and thus drive lithium enhancement via the Cameron & Fowler (1971) mechanism. It has also been proposed by Zhang et al. (2020) and Mallick et al. (2022) that lithium enhancement could result from mergers between RGB stars and white dwarf companions.

We derived the radial velocity (RV) of J0524−0336 (as explained in detailed in Section 2) from three different spectroscopic observational epochs of J0524−0336 over several years, and compared it to the Gaia DR3 radial velocity. We found an excellent agreement within $< 2\,\mathrm{km\,s^{-1}}$, which excludes any radial velocity variation, thus excluding at the present any evidence for a binary companion to our star.

Nevertheless, H_{α} emission profile changes and IR-excesses have been suggested to be due to binary mergers that trigger mass loss events (Castellani & Castellani 1993; Zhang & Jeffery 2013) In this case, excess in near-IR colors will be detected if the material was ejected recently (Mallick et al. 2022). This signifies the possibility, that while no present binary component has been detected for J0524−0336, it might have experienced a recent binary merger that could have invoked extra mixing, leading to enhanced rotation and mass-loss events,

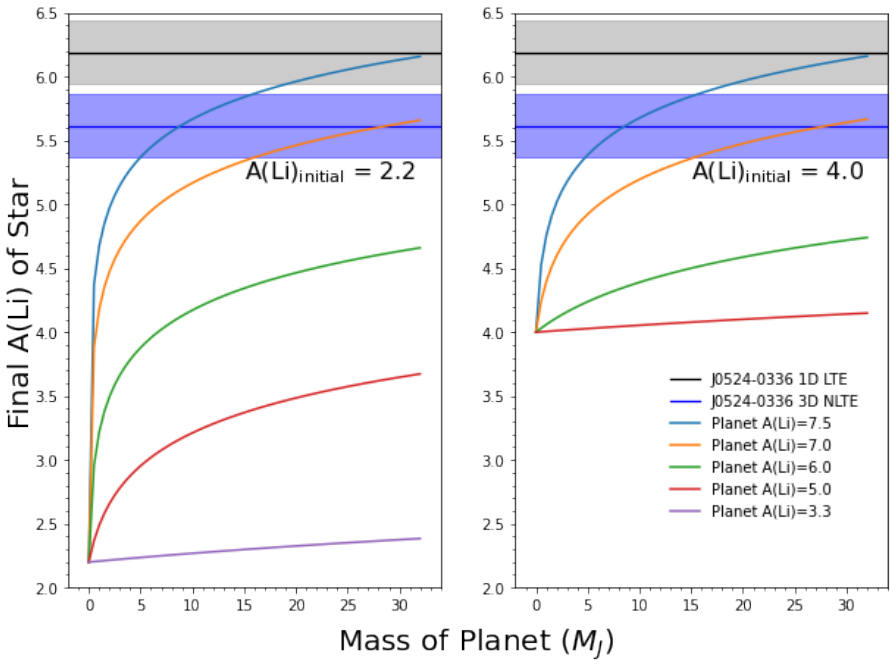

Figure 8. Final Li abundance after a theoretical planetary engulfment event, based on models from from Carlberg et al. (2012), starting with an initial stellar Li abundance of A(Li)=2.2 (left panel), and a super high initial abundance (possibly due to enhanced internal mixing) of A(Li)=4.0 (right panel), as a function of planet mass.

as evidenced by the detection of variable emission in the H_α profile, and IR-flux excess.

6.2. *Internal Mixing*

Lithium production in red giants requires a mechanism to transport ^{3}He inwards from the stellar convective envelope to the deeper and hotter radiation layers where the pp-II chain produces fresh ^{7}Be, and then to transport ^{7}Be outwards so that its electron capture to ^{7}Li occurs in cooler regions where ^{7}Li can not burn (the so-called Cameron-Fowler process; Cameron & Fowler 1971). Although the general idea is well understood and several driving mixing processes have been proposed, the physical origin of the transport mechanism is far from being clear.

As initially shown by Sackmann & Boothroyd (1992), the amount of Li that can potentially be produced in evolved stars strongly depends on the assumed speed and geometry of the driving mixing mechanism as well as on its episodicity, but it is independent of the previous ^{7}Li depletion history of the stars. Yan et al. (2018) revisited this seminal work, using updated nuclear reaction rates and asymmetric parameters for the upwards and downwards mixing flows between the base of the convective envelope and the ^{7}Be production layers. Their fine-tuning model was able to reproduce the Li abundance (A(Li)=4.51) of their star, TYC 429−2097-1, which is more massive and more metal-rich (M=1.43±0.55 $M_\odot$, [Fe/H]=-0.36±0.06) than J0524−0336, and which is lying at the RGB bump (this was established by the authors based on Gaia DR1 parameters, and we checked that it is still the case with Gaia DR2; no DR3 values available). However, their parametric model only allowed for a maximum lithium abundance of A(Li)= 5.07, which is a factor of $\sim$ 3.5 below that of J0524−0336. We speculate that this small difference could be due to the differences in mass and metallicity between the two stars, calling for the same transport process to be more efficient in more metal-poor giants. This was actually already anticipated based on the observed ^{12}C/^{13}C behavior along the RGB, which reveals the role of molecular weight gradient in the development of transport processes such as the thermohaline mixing in red giants (Charbonnel et al. 1998; Charbonnel & Zahn 2007; Lagarde et al. 2012, 2019).

6.2.1. *Lithium Flash*

The scarcity of extremely Li-rich red giants like J0524−0336 and TYC 429−2097-1 calls for these stars being caught during a very brief episode at the beginning of the Li enrichment phase, as originally proposed to occur at the RGB bump and/or during the early-AGB by Charbonnel & Balachandran (2000). The occurrence of this so-called Li-flash was first modelled around the RGB bump by Palacios et al. (2001). They suggested that rotation-induced mixing, which they

were then modeling with a very simplified formalism, would drive the Cameron-Fowler process, leading to the formation a very thin, short-lived lithium-burning shell (Li-BS) in the outskirts of the hydrogen-burning shell. They showed that under certain assumptions for the mixing efficiency, the amount of nuclear energy released in the Li-BS is such that a thermal instability can be ignited. Convection then develops in the thermally unstable layers to carry out the energy, which allows the quasi-instantaneous transport of fresh ^{7}Be towards the convective envelope. During this short-lived ($\sim 2 \times 10^4$ yrs) Li flash, the total stellar luminosity temporarily increases by a factor of ~ 5 in their model. This causes a near doubling of the mass loss, which could potentially form a dust shell around the lithium rich star. Once the thermal instability is quenched, the stellar luminosity decreases to its original bump value. The transport efficiency decreases simultaneously, and the stellar envelope is not fed any more with fresh ^{7}Be. The Li abundance and the carbon isotope ratio start to decrease, under e.g., the influence of thermohaline mixing. Whether this mechanism (which efficiency is strongly debated, see e.g., Harrington & Garaud 2019, and references therein), or any other instability in rotating stars could be the original trigger of the Li-flash at the RGB bump and/or on the early-AGB, remains to be studied.

We see evidence of many aspects of this process in the spectrum of J0524−0336 and of TYC 429−2097−1: (i) the stars' evolutionary status, as defined by their stellar parameters, is compatible with the two stages at which the Lithium Flash is expected to occur; we note in particular that the stellar luminosity of J0524−0336 is a factor of $\sim$ 5 brighter than the location of the RGB bump predicted by our model, and a factor of ~ 2 brighter than the beginning of the early-AGB; TYC 429−2097−1 is at the RGB bump; (ii) the unusually high projected rotational velocity ($v_{\sin i} \sim 11 \mathrm{km\,s^{-1}}$ in both J0524−0336 and TYC 429−2097−1) suggests that the transport mechanism simultaneous extracts angular momentum from the stellar interior; (iii) the $^{12}C/^{13}C \sim 10$ ratio in J0524−0336 (12 in TYC 429−2097−1) indicates a decrease below the post-dredge up value (possibly due to thermohaline mixing) as observed in the majority of bright low-mass red giants; it is also possible that J0524−0336 has acquired its low carbon isotopic value at the RGB bump and is presently undergoing the Li flash on the early-AGB; (iv) the detection of IR-excess colors, as well as the strong and variable emission in the H$_\alpha$ wing profile of J0524−0336 indicates the presence of a dust shell which could result from enhanced mass loss during the Li flash; we note however that no IR excess was found for TYC 429−2097−1; (v) the uniquely ultra lithium abundance observed in J0524−0336 which requires an extremely efficient transport of ^{7}Be in its convective envelope; the Li abundance of TYC 429−2097−1, which is one order of magnitude below that of J0524−0336 , is however still one order of magnitude above the meteoritic value. It is thus possible that both J0524−0336 and TYC 429−2097−1 are indeed just undergoing the *lithium flash*.

7. SUMMARY AND CONCLUSIONS

We report on the discovery of J0524−0336, an ultra Li-rich star, with A(Li)(3D, NLTE)=5.62 and [Li/Fe]=+7.00, from 4 strong lithium absorption lines. To our knowledge, this is the most Li-rich giant star discovered to date. Additionally, we derive abundances of 16 neutron capture elements in J0524−0336 with [Eu/Fe]= +1.34, classifying it as a highly enhanced *r*-process star (rII - [Eu/Fe]$>$ 0.7; Holmbeck et al. 2020). We conduct a detailed stellar parameters analysis of our star using a high-resolution ($R \sim 35,000$), high S/N spectrum. Based on its stellar parameters and Gaia DR3 distance, we find that J0524−0336 lies either on the RGB between the bump and the tip, or on the early-AGB. In any case, it is not currently undergoing core He-burning, which is predicted to occur at a much higher temperature for such a low-mass, low-metallicity star. The star should thus have a relatively low asymptotic period spacing of g-modes. Additionally, we determine a fast projected rotational velocity, $v_{\sin i} \sim 11 \mathrm{km\,s^{-1}}$, as compared to typical values in red giant stars. Furthermore, both an IR-excess, as well as variable emission in the wings of the H$_\alpha$ profile were detected.

We investigated both internal and external processes of possible lithium enhancement that might explain such an ultra-high lithium abundance in a red giant star. Fast rotational velocity could point toward an external source of enrichment, either due to a sub-stellar companion (e.g., planetary) engulfment or binary interaction. No variation was detected in the star's radial velocity over several observational epochs, from which no present binary companion can be inferred. Nevertheless, H$_\alpha$ emission and IR-excess has been postulated to be due to mass-loss events due to a binary merger with giant stars. We show that a sub-stellar companion engulfment cannot produce the Li abundance observed in J0524−0336, and that a scenario in which this would be possible would require a high planetary mass ($M_p \geq 10 \mathrm{M}_J$) and an unrealistically high intrinsic planetary Li content (A$_p$(Li)$>$ 7). On the other hand, it could be possible that the ultra high Li in J0524−0336 could be due to a previous merger with a binary star triggering

and Li-producing extra mixing in the star. Additional studies on the exact amount of Li that could be produced during these interactions are, however, needed to confirm or refute such an event in J0524−0336.

We also investigate possible mixing mechanisms that could drive the so-called Cameron-Fowler process in the radiative layers between the H-burning shell and the convective envelope of J0524−0336, and account for its extreme Li abundance. Recent parametric models, taking into account asymmetric upwards and downwards mixing flows and updated nuclear reaction rates, could reach A(Li)=5.07 for the case of a more massive and more metal-rich red giant sitting at the RGB bump. Similar computations should be done for the case of a low-metallicity, low-mass star such as J0524−0336, to investigate the mass and metallicity dependence of the driving mixing mechanism. We also considered the possibility of Li production in J0524−0336 during the *lithium flash* as proposed by Palacios et al. (2001), and which is expected to occur at the RGB bump and/or on the early-AGB (Charbonnel & Balachandran 2000). J0524−0336's evolutionary status, fast rotational velocity of $v_{\sin i} \sim 11\,\mathrm{km\,s^{-1}}$, IR excess, H_α emission, and unusually high lithium content are predicted indicators of the lithium flash as described in Palacios et al. (2001). It is therefore possible that J0524−0336 was observed during this rare phenomenon, as well as TYC 429-2097-1, which is the next highest A(Li) red giant star, and which is sitting at the bump. However, additional models and upper limits on the production of Li during the Li flash (preferably in 3D), are needed to confirm this scenario.

J0524−0336 sets a new benchmark for lithium-rich metal-poor stars, being the first giant discovered with an A(Li)> 5.0 and [Li/Fe]> +6. It provides a great opportunity to investigate the origin and evolution of Li in the Galaxy, and could be the first of a new population of ultra-rich lithium-enhanced stars expected to be discovered in current and future high-resolution spectroscopic surveys such as the *R*-Process Alliance, as well as others. Asteroseismologic follow-up of metal-poor Li-rich targets will be key to pin down the exact evolutionary status of our and similar stars. However, distinguishing whether J0524−0336 is climbing the RGB or the early-AGB would be extremely challenging, since the global asteroseismic parameters should not differ significantly between these two evolution phases. Finally, we hope that the discovery of J0524−0336 will open a new avenue to understand the instabilities that can develop and transport matter and angular momentum in red giant stars.

We thank Laurent Eyer for very helpful discussion on the *Gaia* parameters of our star. J.K. thanks the University of Florida and the Center for Undergraduate Research and the University Scholars Program for funding his research. R.E. acknowledges support from NSF grant AST-2206263. CC acknowledges support by the Swiss National Science Foundation (Project 200020-192039) and thanks N.Lagarde for useful discussions. I.U.R. acknowledges support from the NSF, grants AST 1815403/1815767, and the NASA Astrophysics Data Analysis Program, grant 80NSSC21K0627. A.F. acknowledges support from NSF grant AST-1716251. We acknowledge support from JINA-CEE (Joint Institute for Nuclear Astrophysics - Center for the Evolution of the Elements), funded by the NSF under Grant No. PHY-1430152. The work of V.M.P. is supported by NOIRLab, which is managed by the Association of Universities for Research in Astronomy (AURA) under a cooperative agreement with the National Science Foundation. TTH acknowledges support from the Swedish Research Council (VR 2021-05556). We also thank Peter Hoeflich and Pavel Dennisenkov for helpful discussions.

This work made use of NASA's Astrophysics Data System Bibliographic Services, and the SIMBAD database, operated at CDS, Strasbourg, France (Wenger et al. 2000). This work has made use of data from the European Space Agency (ESA) mission *Gaia* (https://www.cosmos.esa.int/gaia), processed by the *Gaia* Data Processing and Analysis Consortium (DPAC, https://www.cosmos.esa.int/web/gaia/dpac/consortium).

Facilities: Magellan-Clay (MIKE, Bernstein et al. 2003)

Software: IRAF (Tody 1993), matplotlib (Hunter 2007), MOOG (Sneden 1973; Sobeck et al. 2011) , LOTUS (Li & Ezzeddine 2022)

REFERENCES

1989, ApJS, 71, 293, doi: 10.1086/191375

Adamów, M., Niedzielski, A., Villaver, E., et al. 2015, A&A, 581, A94, doi: 10.1051/0004-6361/201526582

Adamów, M., Niedzielski, A., Villaver, E., Wolszczan, A., & Nowak, G. 2014, A&A, 569, A55, doi: 10.1051/0004-6361/201423400

Aguilera-Gómez, C., Chanamé, J., Pinsonneault, M. H., & Carlberg, J. K. 2016, ApJ, 829, 127, doi: 10.3847/0004-637X/829/2/127

Aguilera-Gómez, C., Chanamé, J., Pinsonneault, M. H., & Carlberg, J. K. 2016, The Astrophysical Journal, 829, 127, doi: 10.3847/0004-637x/829/2/127

Aguilera-Gómez, C., Monaco, L., Mucciarelli, A., et al. 2022, A&A, 657, A33, doi: 10.1051/0004-6361/202141750

Aguilera-Gómez, C., Chanamé, J., & Pinsonneault, M. H. 2020, The Astrophysical Journal, 897, L20, doi: 10.3847/2041-8213/ab9d26

Alcalá, J. M., Biazzo, K., Covino, E., Frasca, A., & Bedin, L. R. 2011, A&A, 531, L12, doi: 10.1051/0004-6361/201117174

Alexander, J. B. 1967, The Observatory, 87, 238

Amarsi, A. M., Lind, K., Asplund, M., Barklem, P. S., & Collet, R. 2016, MNRAS, 463, 1518, doi: 10.1093/mnras/stw2077

Andrievsky, S. M., Gorlova, N. I., Klochkova, V. G., Kovtyukh, V. V., & Panchuk, V. E. 1999, Astronomische Nachrichten, 320, 35

Anthony-Twarog, B. J., Deliyannis, C. P., Rich, E., & Twarog, B. A. 2013, ApJL, 767, L19, doi: 10.1088/2041-8205/767/1/L19

Asplund, M., Grevesse, N., Sauval, A. J., & Scott, P. 2009, ARA&A, 47, 481, doi: 10.1146/annurev.astro.46.060407.145222

Bailer-Jones, C. A. L., Rybizki, J., Fouesneau, M., Demleitner, M., & Andrae, R. 2021, AJ, 161, 147, doi: 10.3847/1538-3881/abd806

Balachandran, S. C., Fekel, F. C., Henry, G. W., & Uitenbroek, H. 2000, ApJ, 542, 978, doi: 10.1086/317055

Barklem, P. S. 2018, A&A, 612, A90, doi: 10.1051/0004-6361/201732365

Bergemann, M., & Cescutti, G. 2010, A&A, 522, A9, doi: 10.1051/0004-6361/201014250

Bernstein, R., Shectman, S. A., Gunnels, S. M., Mochnacki, S., & Athey, A. E. 2003, in Proc. SPIE, Vol. 4841, Instrument Design and Performance for Optical/Infrared Ground-based Telescopes, ed. M. Iye & A. F. M. Moorwood, 1694–1704, doi: 10.1117/12.461502

Bharat Kumar, Y., Reddy, B. E., Muthumariappan, C., & Zhao, G. 2015, A&A, 577, A10, doi: 10.1051/0004-6361/201425076

Binks, A. S., Jeffries, R. D., Sacco, G. G., et al. 2022, MNRAS, 513, 5727, doi: 10.1093/mnras/stac1245

Brown, J. A., Sneden, C., Lambert, D. L., & Dutchover, Edward, J. 1989, ApJS, 71, 293, doi: 10.1086/191375

Bruntt, H., Bedding, T. R., Quirion, P. O., et al. 2010, MNRAS, 405, 1907, doi: 10.1111/j.1365-2966.2010.16575.x

Cameron, A. G. W., & Fowler, W. A. 1971, ApJ, 164, 111, doi: 10.1086/150821

Canto Martins, B. L., Lèbre, A., de Laverny, P., et al. 2006, A&A, 451, 993, doi: 10.1051/0004-6361:20053334

Canto Martins, B. L., Lèbre, A., Palacios, A., et al. 2011, A&A, 527, A94, doi: 10.1051/0004-6361/201015015

Carlberg, J. K., Cunha, K., Smith, V. V., & Majewski, S. R. 2012, The Astrophysical Journal, 757, 109, doi: 10.1088/0004-637x/757/2/109

Carlberg, J. K., Smith, V. V., Cunha, K., Majewski, S. R., & Rood, R. T. 2010, ApJL, 723, L103, doi: 10.1088/2041-8205/723/1/L103

Carlberg, J. K., Smith, V. V., Cunha, K., et al. 2015, ApJ, 802, 7, doi: 10.1088/0004-637X/802/1/7

Carlsson, M. 1986, Uppsala Astronomical Observatory Reports, 33

Carlsson, M. 1992, in Astronomical Society of the Pacific Conference Series, Vol. 26, Cool Stars, Stellar Systems, and the Sun, ed. M. S. Giampapa & J. A. Bookbinder, 499

Carney, B. W., Fry, A. M., & Gonzalez, G. 1998, AJ, 116, 2984, doi: 10.1086/300630

Casagrande, L., Ramírez, I., Meléndez, J., Bessell, M., & Asplund, M. 2010, A&A, 512, A54, doi: 10.1051/0004-6361/200913204

Casagrande, L., Lin, J., Rains, A. D., et al. 2020, Effective temperature calibration from the InfraRed Flux Method in the Gaia system. https://arxiv.org/abs/2011.02517

Casey, A. R. 2014, PhD thesis, Australian National University, doi: 10.5281/zenodo.49493

Casey, A. R., Ruchti, G., Masseron, T., et al. 2016, MNRAS, 461, 3336, doi: 10.1093/mnras/stw1512

Casey, A. R., Ho, A. Y. Q., Ness, M., et al. 2019, The Astrophysical Journal, 880, 125, doi: 10.3847/1538-4357/ab27bf

Castellani, M., & Castellani, V. 1993, ApJ, 407, 649, doi: 10.1086/172547

Castelli, F., & Kurucz, R. L. 2004

Chanamé, J., Pinsonneault, M. H., Aguilera-Gómez, C., & Zinn, J. C. 2022, ApJ, 933, 58, doi: 10.3847/1538-4357/ac70c8

Charbonneau, P., & Michaud, G. 1990, ApJ, 352, 681, doi: 10.1086/168570

Charbonnel, C., & Balachandran, S. C. 2000, A&A, 359, 563. https://arxiv.org/abs/astro-ph/0005280

Charbonnel, C., Brown, J. A., & Wallerstein, G. 1998, A&A, 332, 204. https://arxiv.org/abs/astro-ph/9712207

Charbonnel, C., Deliyannis, C. P., & Pinsonneault, M. H. 2000, arXiv e-prints, astro. https://arxiv.org/abs/astro-ph/0006280

Charbonnel, C., & Lagarde, N. 2010, A&A, 522, A10, doi: 10.1051/0004-6361/201014432

Charbonnel, C., & Talon, S. 2005, Science, 309, 2189, doi: 10.1126/science.1116849

Charbonnel, C., & Zahn, J. P. 2007, A&A, 467, L15, doi: 10.1051/0004-6361:20077274

Charbonnel, C., Lagarde, N., Jasniewicz, G., et al. 2020, Astronomy & Astrophysics, 633, A34, doi: 10.1051/0004-6361/201936360

Cortés, C., Silva, J. R. P., Recio-Blanco, A., et al. 2009, ApJ, 704, 750, doi: 10.1088/0004-637X/704/1/750

de la Reza, R., Drake, N. A., & da Silva, L. 1996, The Astrophysical Journal, 456, doi: 10.1086/309874

de la Reza, R., Drake, N. A., da Silva, L., Torres, C. A. O., & Martin, E. L. 1997, ApJL, 482, L77, doi: 10.1086/310685

De Silva, G. M., Freeman, K. C., Bland-Hawthorn, J., et al. 2015, MNRAS, 449, 2604, doi: 10.1093/mnras/stv327

Deal, M., & Martins, C. J. A. P. 2021, A&A, 653, A48, doi: 10.1051/0004-6361/202140725

Deepak, Lambert, D. L., & Reddy, B. E. 2020, MNRAS, 494, 1348, doi: 10.1093/mnras/staa729

Deliyannis, C. P., Pinsonneault, M. H., & Charbonnel, C. 2000, in The Light Elements and their Evolution, ed. L. da Silva, R. de Medeiros, & M. Spite, Vol. 198, 61

Deng, L.-C., Newberg, H. J., Liu, C., et al. 2012, Research in Astronomy and Astrophysics, 12, 735, doi: 10.1088/1674-4527/12/7/003

Denissenkov, P., & Weiss, A. 2000, Astronomy and Astrophysics, 358

Denissenkov, P. A., & Herwig, F. 2004, ApJ, 612, 1081, doi: 10.1086/422575

D'Orazi, V., Gratton, R. G., Angelou, G. C., et al. 2015, ApJL, 801, L32, doi: 10.1088/2041-8205/801/2/L32

Drake, N. A., de la Reza, R., da Silva, L., & Lambert, D. L. 2002, AJ, 123, 2703, doi: 10.1086/339968

Dumont, T., Charbonnel, C., Palacios, A., & Borisov, S. 2021a, A&A, 654, A46, doi: 10.1051/0004-6361/202141094

Dumont, T., Palacios, A., Charbonnel, C., et al. 2021b, A&A, 646, A48, doi: 10.1051/0004-6361/202039515

Ezzeddine, R., Frebel, A., & Plez, B. 2017, ApJ, 847, 142, doi: 10.3847/1538-4357/aa8875

Ezzeddine, R., Plez, B., Merle, T., Gebran, M., & Thévenin, F. 2016, ArXiv e-prints. https://arxiv.org/abs/1612.09302

Ezzeddine, R., Rasmussen, K., Frebel, A., et al. 2020, The Astrophysical Journal, 898, 150, doi: 10.3847/1538-4357/ab9d1a

Fekel, F. C., & Watson, L. C. 1998, AJ, 116, 2466, doi: 10.1086/300614

Fischer, D. A., & Valenti, J. 2005, ApJ, 622, 1102, doi: 10.1086/428383

Forestini, M., & Charbonnel, C. 1997, A&AS, 123, 241, doi: 10.1051/aas:1997348

Frebel, A., Casey, A. R., Jacobson, H. R., & Yu, Q. 2013, ApJ, 769, 57, doi: 10.1088/0004-637X/769/1/57

Gaia Collaboration, Prusti, T., de Bruijne, J. H. J., et al. 2016, A&A, 595, A1, doi: 10.1051/0004-6361/201629272

Gao, Q., Shi, J.-R., Yan, H.-L., et al. 2019, ApJS, 245, 33, doi: 10.3847/1538-4365/ab505c

Gonzalez, O. A., Zoccali, M., Monaco, L., et al. 2009, A&A, 508, 289, doi: 10.1051/0004-6361/200912469

Gratton, R. G., & D'Antona, F. 1989, A&A, 215, 66

Gratton, R. G., Sneden, C., Carretta, E., & Bragaglia, A. 2000, A&A, 354, 169

Gruyters, P., Lind, K., Richard, O., et al. 2016, A&A, 589, A61, doi: 10.1051/0004-6361/201527948

Gustafsson, B., Bell, R. A., Eriksson, K., & Nordlund, A. 1975, A&A, 42, 407

Gustafsson, B., Edvardsson, B., Eriksson, K., et al. 2008, A&A, 486, 951, doi: 10.1051/0004-6361:200809724

Hanni, L. 1984, Soviet Astronomy Letters, 10, 51

Hansen, T. T., Holmbeck, E. M., Beers, T. C., et al. 2018, ApJ, 858, 92, doi: 10.3847/1538-4357/aabacc

Harrington, P. Z., & Garaud, P. 2019, ApJL, 870, L5, doi: 10.3847/2041-8213/aaf812

Hekker, S., & Meléndez, J. 2007, Astronomy & Astrophysics, 475, 1003–1009, doi: 10.1051/0004-6361:20078233

Hill, V., & Pasquini, L. 1999, A&A, 348, L21. https://arxiv.org/abs/astro-ph/9907106

Holmbeck, E. M., Hansen, T. T., Beers, T. C., et al. 2020, ApJS, 249, 30, doi: 10.3847/1538-4365/ab9c19

Hunter, J. D. 2007, Computing in Science & Engineering, 9, 90, doi: 10.1109/MCSE.2007.55

Iben, Icko, J. 1967, ApJ, 147, 624, doi: 10.1086/149040
Jasniewicz, G., Parthasarathy, M., de Laverny, P., & Thévenin, F. 1999a, A&A, 342, 831
—. 1999b, A&A, 342, 831
Ji, A. P., Frebel, A., Simon, J. D., & Chiti, A. 2016, The Astrophysical Journal, 830, 93, doi: 10.3847/0004-637X/830/2/93
Jofré, E., Petrucci, R., García, L., & Gómez, M. 2015, A&A, 584, L3, doi: 10.1051/0004-6361/201527337
Keeping, E. S. 1962, Princeton, NJ: Van Nostrand
Kelson, D. D. 2003, PASP, 115, 688, doi: 10.1086/375502
Kirby, E. N., Fu, X., Guhathakurta, P., & Deng, L. 2012, ApJL, 752, L16, doi: 10.1088/2041-8205/752/1/L16
Kirby, E. N., Guhathakurta, P., Zhang, A. J., et al. 2016, ApJ, 819, 135, doi: 10.3847/0004-637X/819/2/135
Korn, A. J., Grundahl, F., Richard, O., et al. 2006, Nature, 442, 657, doi: 10.1038/nature05011
Kumar, Y. B., & Reddy, B. E. 2020, Journal of Astrophysics and Astronomy, 41, 49, doi: 10.1007/s12036-020-09660-9
Kumar, Y. B., Reddy, B. E., & Lambert, D. L. 2011, The Astrophysical Journal, 730, L12, doi: 10.1088/2041-8205/730/1/l12
Kumar, Y. B., Reddy, B. E., & Lambert, D. L. 2011, ApJL, 730, L12, doi: 10.1088/2041-8205/730/1/L12
Lagarde, N., Decressin, T., Charbonnel, C., et al. 2012, A&A, 543, A108, doi: 10.1051/0004-6361/201118331
Lagarde, N., Reylé, C., Robin, A. C., et al. 2019, A&A, 621, A24, doi: 10.1051/0004-6361/201732433
Lèbre, A., de Laverny, P., de Medeiros, J. R., Charbonnel, C., & da Silva, L. 1999, A&A, 345, 936
Lèbre, A., Palacios, A., Do Nascimento, J. D., J., et al. 2009, A&A, 504, 1011, doi: 10.1051/0004-6361/200912038
Li, Y., & Ezzeddine, R. 2022, LOTUS: 1D Non-LTE stellar parameter determination via Equivalent Width method, Astrophysics Source Code Library, record ascl:2207.017. http://ascl.net/2207.017
Lind, K., Asplund, M., Barklem, P. S., & Belyaev, A. K. 2011, A&A, 528, A103, doi: 10.1051/0004-6361/201016095
Lind, K., Bergemann, M., & Asplund, M. 2012, MNRAS, 427, 50, doi: 10.1111/j.1365-2966.2012.21686.x
Lind, K., Melendez, J., Asplund, M., Collet, R., & Magic, Z. 2013, A&A, 554, A96, doi: 10.1051/0004-6361/201321406
Lind, K., Primas, F., Charbonnel, C., Grundahl, F., & Asplund, M. 2009, A&A, 503, 545, doi: 10.1051/0004-6361/200912524
Liu, Y. J., Tan, K. F., Wang, L., et al. 2014a, ApJ, 785, 94, doi: 10.1088/0004-637X/785/2/94
—. 2014b, ApJ, 785, 94, doi: 10.1088/0004-637X/785/2/94
Luck, R. E. 1982, PASP, 94, 811, doi: 10.1086/131068
Lyubimkov, L. S. 2016, Astrophysics, 59, 411, doi: 10.1007/s10511-016-9446-5
Lyubimkov, L. S., Lambert, D. L., Kaminsky, B. M., et al. 2012, MNRAS, 427, 11, doi: 10.1111/j.1365-2966.2012.21617.x
Magrini, L., Lagarde, N., Charbonnel, C., et al. 2021a, A&A, 651, A84, doi: 10.1051/0004-6361/202140935
Magrini, L., Smiljanic, R., Franciosini, E., et al. 2021b, A&A, 655, A23, doi: 10.1051/0004-6361/202141275
Mallick, A., Reddy, B. E., & Muthumariappan, C. 2022, MNRAS, 511, 3741, doi: 10.1093/mnras/stac224
Martell, S., Simpson, J., Balasubramaniam, A., et al. 2020, The GALAH survey: Lithium-rich giant stars require multiple formation channels. https://arxiv.org/abs/2006.02106
Martell, S. L., & Shetrone, M. D. 2013, MNRAS, 430, 611, doi: 10.1093/mnras/sts661
Martell, S. L., Simpson, J. D., Balasubramaniam, A. G., et al. 2021, Monthly Notices of the Royal Astronomical Society, doi: 10.1093/mnras/stab1356
Mashonkina, L. I., Sitnova, T. N., & Pakhomov, Y. V. 2016, Astronomy Letters, 42, 606, doi: 10.1134/S1063773716080028
McWilliam, A., & Rich, R. M. 1994, ApJS, 91, 749, doi: 10.1086/191954
Monaco, L., Villanova, S., Moni Bidin, C., et al. 2011a, A&A, 529, A90, doi: 10.1051/0004-6361/201016285
—. 2011b, A&A, 529, A90, doi: 10.1051/0004-6361/201016285
Monaco, L., Boffin, H. M. J., Bonifacio, P., et al. 2014, A&A, 564, L6, doi: 10.1051/0004-6361/201323348
Mori, K., Kusakabe, M., Balantekin, A. B., Kajino, T., & Famiano, M. A. 2021, MNRAS, 503, 2746, doi: 10.1093/mnras/stab595
Mucciarelli, A., Monaco, L., Bonifacio, P., et al. 2022, A&A, 661, A153, doi: 10.1051/0004-6361/202142889
Nordlander, T., Korn, A. J., Richard, O., & Lind, K. 2012, ApJ, 753, 48, doi: 10.1088/0004-637X/753/1/48
Nordlander, T., & Lind, K. 2017, A&A, 607, A75, doi: 10.1051/0004-6361/201730427
Osorio, Y., Barklem, P. S., Lind, K., et al. 2015, A&A, 579, A53, doi: 10.1051/0004-6361/201525846
Palacios, A., Charbonnel, C., & Forestini, M. 2001, A&A, 375, L9, doi: 10.1051/0004-6361:20010903
Placco, V. M., Frebel, A., Beers, T. C., & Stancliffe, R. J. 2014, ApJ, 797, 21, doi: 10.1088/0004-637X/797/1/21
Placco, V. M., Sneden, C., Roederer, I. U., et al. 2021, Research Notes of the American Astronomical Society, 5, 92, doi: 10.3847/2515-5172/abf651

Rebull, L. M., Carlberg, J. K., Gibbs, J. C., et al. 2015, AJ, 150, 123, doi: 10.1088/0004-6256/150/4/123
Reed, B. C. 1998, JRASC, 92, 36
Reimers, D. 1975, Memoires of the Societe Royale des Sciences de Liege, 8, 369
Reyniers, M., & Van Winckel, H. 2001, A&A, 365, 465, doi: 10.1051/0004-6361:20000146
Richard, O., Michaud, G., & Richer, J. 2005, ApJ, 619, 538, doi: 10.1086/426470
Roederer, I. U., Hattori, K., & Valluri, M. 2018, AJ, 156, 179, doi: 10.3847/1538-3881/aadd9c
Roederer, I. U., Preston, G. W., Thompson, I. B., et al. 2014, AJ, 147, 136, doi: 10.1088/0004-6256/147/6/136
Roederer, I. U., Preston, G. W., Thompson, I. B., et al. 2014, The Astronomical Journal, 147, 136, doi: 10.1088/0004-6256/147/6/136
Roederer, I. U., Sakari, C. M., Placco, V. M., et al. 2018, The Astrophysical Journal, 865, 129, doi: 10.3847/1538-4357/aadd92
Ruchti, G. R., Fulbright, J. P., Wyse, R. F. G., et al. 2011, ApJ, 743, 107, doi: 10.1088/0004-637X/743/2/107
Sackmann, I. J., & Boothroyd, A. I. 1992, ApJL, 392, L71, doi: 10.1086/186428
—. 1999, ApJ, 510, 217, doi: 10.1086/306545
Sakari, C. M., Placco, V. M., Farrell, E. M., et al. 2018, ApJ, 868, 110, doi: 10.3847/1538-4357/aae9df
Schlafly, E. F., & Finkbeiner, D. P. 2011, ApJ, 737, 103, doi: 10.1088/0004-637X/737/2/103
Siess, L., & Livio, M. 1999, MNRAS, 308, 1133, doi: 10.1046/j.1365-8711.1999.02784.x
Silva Aguirre, V., Ruchti, G. R., Hekker, S., et al. 2014, ApJL, 784, L16, doi: 10.1088/2041-8205/784/1/L16
Singh, R., Reddy, B. E., & Kumar, Y. B. 2019, MNRAS, 482, 3822, doi: 10.1093/mnras/sty2939
Skrutskie, M. F., Cutri, R. M., Stiening, R., et al. 2006, AJ, 131, 1163, doi: 10.1086/498708
Smiljanic, R., Franciosini, E., Bragaglia, A., et al. 2018, A&A, 617, A4, doi: 10.1051/0004-6361/201833027
Smith, V. V., Shetrone, M. D., & Keane, M. J. 1999, ApJL, 516, L73, doi: 10.1086/312011
Sneden, C., Cowan, J. J., & Gallino, R. 2008, ARA&A, 46, 241, doi: 10.1146/annurev.astro.46.060407.145207
Sneden, C., Cowan, J. J., & Gallino, R. 2008, Annual Review of Astronomy and Astrophysics, 46, 241, doi: 10.1146/annurev.astro.46.060407.145207
Sneden, C. A. 1973, PhD thesis, University of Texas at Austin
Sobeck, J. S., Kraft, R. P., Sneden, C., et al. 2011, AJ, 141, 175, doi: 10.1088/0004-6256/141/6/175
Soderblom, D. R., Fedele, S. B., Jones, B. F., Stauffer, J. R., & Prosser, C. F. 1993, AJ, 106, 1080, doi: 10.1086/116705
Strassmeier, K. G., Carroll, T. A., Weber, M., & Granzer, T. 2015, A&A, 574, A31, doi: 10.1051/0004-6361/201424130
Takeda, Y., Zhao, G., Chen, Y.-Q., Qiu, H.-M., & Takada-Hidai, M. 2002, PASJ, 54, 275, doi: 10.1093/pasj/54.2.275
Talon, S., & Charbonnel, C. 2010, in Light Elements in the Universe, ed. C. Charbonnel, M. Tosi, F. Primas, & C. Chiappini, Vol. 268, 365–374, doi: 10.1017/S1743921310004485
Tody, D. 1986, in Society of Photo-Optical Instrumentation Engineers (SPIE) Conference Series, Vol. 627, Instrumentation in astronomy VI, ed. D. L. Crawford, 733, doi: 10.1117/12.968154
Tody, D. 1993, Astronomical Society of the Pacific Conference Series, Vol. 52, IRAF in the Nineties, ed. R. J. Hanisch, R. J. V. Brissenden, & J. Barnes, 173
Tognelli, E., Degl'Innocenti, S., Prada Moroni, P. G., et al. 2021, Frontiers in Astronomy and Space Sciences, 8, 22, doi: 10.3389/fspas.2021.604872
Vassiliadis, E., & Wood, P. R. 1993, ApJ, 413, 641, doi: 10.1086/173033
Wallerstein, G., & Sneden, C. 1982a, ApJ, 255, 577, doi: 10.1086/159859
—. 1982b, ApJ, 255, 577, doi: 10.1086/159859
Wang, E. X., Nordlander, T., Asplund, M., et al. 2021, MNRAS, 500, 2159, doi: 10.1093/mnras/staa3381
Wenger, M., Ochsenbein, F., Egret, D., et al. 2000, A&AS, 143, 9, doi: 10.1051/aas:2000332
Wright, E. L., Eisenhardt, P. R. M., Mainzer, A. K., et al. 2010, AJ, 140, 1868, doi: 10.1088/0004-6256/140/6/1868
Yan, H.-L., Shi, J.-R., Zhou, Y.-T., et al. 2018, Nature Astronomy, 2, 790, doi: 10.1038/s41550-018-0544-7
Yan, H.-L., Zhou, Y.-T., Zhang, X., et al. 2020, Nature Astronomy, 5, 86–93, doi: 10.1038/s41550-020-01217-8
Yan, H.-L., Zhou, Y.-T., Zhang, X., et al. 2021, Nature Astronomy, 5, 86, doi: 10.1038/s41550-020-01217-8
Yong, D., Norris, J. E., Bessell, M. S., et al. 2013, ApJ, 762, 26, doi: 10.1088/0004-637X/762/1/26
Zhang, X., & Jeffery, C. S. 2013, MNRAS, 430, 2113, doi: 10.1093/mnras/stt035
Zhang, X., Jeffery, C. S., Li, Y., & Bi, S. 2020, The Astrophysical Journal, 889, 33, doi: 10.3847/1538-4357/ab5e89
Zhou, Y. T., Shi, J. R., Yan, H. L., et al. 2018, A&A, 615, A74, doi: 10.1051/0004-6361/201730389

Table 6. Line by Line Element Abundances

λ (Å)	Species	χ (eV)	$\log gf$	EW (mÅ)	log ϵ(X) (dex)
6300.30	O I	0.00	−9.82	30.15	7.41
4167.27	Mg I	4.35	−0.71	65.42	5.51
4571.09	Mg I	0.00	−5.68	135.03	6.09
4702.99	Mg I	4.33	−0.38	105.49	5.60
5172.68	Mg I	2.71	−0.45	310.27	5.70
5183.60	Mg I	2.72	−0.23	363.18	5.70
5528.40	Mg I	4.34	−0.49	118.84	5.78
5711.09	Mg I	4.34	−1.72	21.35	5.51
3961.52	Al I	0.01	−0.34	170.81	< 3.53
4102.93	Si I	1.91	−3.14	131.52	6.10
5708.39	Si I	4.93	−1.47	16.96	5.76
7664.90	K I	0.00	0.13	112.55	3.32
7698.96	K I	0.00	−0.16	82.34	3.21
4425.44	Ca I	1.88	−0.35	62.39	3.96
4454.78	Ca I	1.90	0.26	131.61	4.66
5265.55	Ca I	2.52	−0.26	63.30	4.52
5349.46	Ca I	2.71	−0.31	20.74	4.03
5581.97	Ca I	2.52	−0.55	26.55	4.17
5588.76	Ca I	2.52	0.21	79.56	4.26
5590.12	Ca I	2.52	−0.57	17.39	3.95
5594.48	Ca I	2.52	0.09	66.63	4.17
5598.48	Ca I	2.52	−0.08	55.24	4.18
5601.28	Ca I	2.53	−0.52	23.28	4.06
5857.45	Ca I	2.93	0.23	43.16	4.16
6102.72	Ca I	1.88	−0.79	75.21	4.33
6122.22	Ca I	1.89	−0.31	117.88	4.51
6162.17	Ca I	1.90	−0.08	138.57	4.61
6169.05	Ca I	2.52	−0.79	17.04	4.13
6169.55	Ca I	2.53	−0.47	28.28	4.09
6439.07	Ca I	2.52	0.47	98.82	4.20
6449.81	Ca I	2.52	−0.50	34.06	4.19
6499.64	Ca I	2.52	−0.81	16.79	4.12
6717.68	Ca I	2.71	−0.52	26.98	4.29
4314.08	Sc II	0.62	−0.10	160.44	1.61
4324.99	Sc II	0.59	−0.44	143.71	1.55
4400.38	Sc II	0.61	−0.54	125.07	1.24
4415.54	Sc II	0.59	−0.67	127.64	1.39
5239.81	Sc II	1.46	−0.77	48.47	0.99
5526.78	Sc II	1.77	0.02	67.79	0.83
5641.00	Sc II	1.50	−1.13	23.56	0.92
5657.90	Sc II	1.51	−0.60	55.80	0.94
5684.21	Sc II	1.51	−1.07	27.35	0.95
6604.57	Sc II	1.36	−1.31	20.49	0.77
3761.32	Ti II	0.57	0.18	232.61	3.19
3913.46	Ti II	1.12	−0.42	179.94	3.72

Table 6 continued

Table 6 *(continued)*

λ (Å)	Species	χ (eV)	$\log gf$	EW (mÅ)	log ϵ(X) (dex)
4028.33	Ti II	1.89	−0.96	58.23	2.53
4053.82	Ti II	1.89	−1.21	33.77	2.33
4161.52	Ti II	1.08	−2.16	82.40	3.11
4163.63	Ti II	2.59	−0.40	62.77	2.88
5669.05	Sc II	1.50	−1.20	24.74	1.01
4184.30	Ti II	1.08	−2.51	55.23	2.96
4330.72	Ti II	1.18	−2.06	76.81	2.95
4337.91	Ti II	1.08	−0.96	174.83	3.75
4394.05	Ti II	1.22	−1.78	68.83	2.56
4395.03	Ti II	1.08	−0.54	198.53	3.69
4395.83	Ti II	1.24	−1.93	64.30	2.67
4399.76	Ti II	1.24	−1.19	125.53	3.13
4417.71	Ti II	1.17	−1.19	144.99	3.44
4418.33	Ti II	1.24	−1.97	78.49	2.94
4441.73	Ti II	1.18	−2.41	57.21	2.94
4443.80	Ti II	1.08	−0.72	173.75	3.42
4444.55	Ti II	1.12	−2.24	80.79	3.10
4450.48	Ti II	1.08	−1.52	121.41	3.13
4464.44	Ti II	1.16	−1.81	85.70	2.80
4470.85	Ti II	1.17	−2.02	80.72	2.92
4488.34	Ti II	3.12	−0.82	12.63	2.79
4468.51	Ti II	1.13	−0.60	199.24	3.78
4493.52	Ti II	1.08	−3.02	31.87	3.00
4501.27	Ti II	1.12	−0.77	183.49	3.65
4529.48	Ti II	1.57	−2.03	66.94	3.19
4563.77	Ti II	1.22	−0.96	171.39	3.71
4589.91	Ti II	1.24	−1.79	106.86	3.24
4636.32	Ti II	1.16	−3.02	21.04	2.83
4657.20	Ti II	1.24	−2.24	73.73	3.05
4708.66	Ti II	1.24	−2.34	56.68	2.88
4779.97	Ti II	2.05	−1.37	58.93	2.95
4798.53	Ti II	1.08	−2.68	70.82	3.21
4805.08	Ti II	2.06	−1.10	76.87	2.97
4865.61	Ti II	1.12	−2.81	46.92	3.02
4911.17	Ti II	3.12	−0.34	19.90	2.49
5005.15	Ti II	1.57	−2.73	14.96	2.83
5129.15	Ti II	1.89	−1.24	73.38	2.77
5185.90	Ti II	1.89	−1.49	61.18	2.83
5188.68	Ti II	1.58	−1.05	142.23	3.39
5336.78	Ti II	1.58	−1.59	89.00	2.93
5381.02	Ti II	1.57	−1.92	66.07	2.90
5418.76	Ti II	1.58	−2.00	44.11	2.67
4289.72	Cr I	0.00	−0.37	188.37	3.71
4545.95	Cr I	0.94	−1.37	32.35	2.96
4580.05	Cr I	0.94	−1.65	33.04	3.24
4600.75	Cr I	1.00	−1.26	48.69	3.19
4616.13	Cr I	0.98	−1.19	48.41	3.09

Table 6 continued

Table 6 *(continued)*

λ (Å)	Species	χ (eV)	$\log gf$	EW (mÅ)	log ϵ(X) (dex)
4626.18	Cr I	0.97	−1.32	39.88	3.06
4646.15	Cr I	1.03	−0.74	81.07	3.24
4651.28	Cr I	0.98	−1.46	29.98	3.03
4652.15	Cr I	1.00	−1.03	54.84	3.05
5247.56	Cr I	0.96	−1.64	36.19	3.21
5296.69	Cr I	0.98	−1.36	50.57	3.18
5298.28	Cr I	0.98	−1.14	77.38	3.36
5300.74	Cr I	0.98	−2.00	12.85	3.04
5345.80	Cr I	1.00	−0.95	79.13	3.21
5348.31	Cr I	1.00	−1.21	51.64	3.06
5409.77	Cr I	1.03	−0.67	95.67	3.23
4034.48	Mn I	0.00	−0.81	182.48	3.51
4754.04	Mn I	2.28	−0.08	35.15	2.58
4783.43	Mn I	2.30	0.04	46.29	2.66
4823.52	Mn I	2.32	0.14	57.80	2.76
3852.57	Fe I	2.18	−1.18	78.01	4.82
3949.95	Fe I	2.18	−1.25	65.56	4.56
4001.66	Fe I	2.18	−1.90	51.11	4.90
4032.62	Fe I	1.49	−2.38	67.30	4.80
4058.21	Fe I	3.21	−1.11	27.83	4.92
4062.44	Fe I	2.85	−0.86	49.74	4.65
4067.97	Fe I	3.21	−0.47	47.51	4.66
4073.76	Fe I	3.27	−0.90	36.24	4.95
4076.62	Fe I	3.21	−0.37	66.66	4.92
4098.17	Fe I	3.24	−0.88	41.33	4.98
4109.80	Fe I	2.85	−0.94	60.44	4.91
4114.44	Fe I	2.83	−1.30	26.73	4.60
4121.80	Fe I	2.83	−1.45	29.13	4.80
4134.67	Fe I	2.83	−0.64	71.54	4.80
4136.99	Fe I	3.42	−0.45	32.64	4.59
4139.92	Fe I	0.99	−3.62	55.77	5.16
4147.66	Fe I	1.48	−2.07	112.74	5.39
4154.49	Fe I	2.83	−0.68	83.85	5.09
4154.80	Fe I	3.37	−0.40	49.67	4.79
4156.79	Fe I	2.83	−0.80	73.25	4.98
4157.78	Fe I	3.42	−0.40	47.66	4.82
4158.79	Fe I	3.43	−0.67	21.66	4.57
4174.91	Fe I	0.91	−2.93	132.56	5.93
4181.75	Fe I	2.83	−0.37	86.72	4.82
4184.89	Fe I	2.83	−0.86	44.61	4.50
4187.03	Fe I	2.45	−0.51	119.64	5.15
4187.79	Fe I	2.42	−0.51	135.57	5.40
4195.32	Fe I	3.33	−0.49	49.55	4.82
4216.18	Fe I	0.00	−3.35	193.17	6.27
4227.42	Fe I	3.33	0.26	99.30	5.07
4233.60	Fe I	2.48	−0.57	98.99	4.80
4238.81	Fe I	3.40	−0.23	49.48	4.63

Table 6 continued

Table 6 *(continued)*

λ (Å)	Species	χ (eV)	$\log gf$	EW (mÅ)	log ϵ(X) (dex)
4260.47	Fe I	2.40	0.07	153.14	5.02
4337.04	Fe I	1.56	−1.69	130.81	5.36
4352.73	Fe I	2.22	−1.29	120.03	5.61
4415.12	Fe I	1.61	−0.62	199.74	5.33
4422.56	Fe I	2.85	−1.11	73.35	5.21
4430.61	Fe I	2.22	−1.65	85.86	5.18
4442.33	Fe I	2.20	−1.22	120.79	5.39
4443.19	Fe I	2.86	−1.04	64.01	4.97
4447.71	Fe I	2.22	−1.33	92.49	4.98
4459.11	Fe I	2.18	−1.27	126.76	5.51
4476.01	Fe I	2.85	−0.82	90.55	5.23
4489.73	Fe I	0.12	−3.89	153.35	6.02
4494.56	Fe I	2.20	−1.14	128.04	5.40
4528.61	Fe I	2.18	−0.82	168.74	5.63
4531.14	Fe I	1.48	−2.10	135.86	5.63
4647.43	Fe I	2.95	−1.35	50.34	5.12
4678.84	Fe I	3.60	−0.83	34.09	5.11
4710.28	Fe I	3.02	−1.61	33.94	5.17
4733.59	Fe I	1.49	−2.98	85.41	5.48
4736.77	Fe I	3.21	−0.75	77.89	5.27
4859.74	Fe I	2.88	−0.76	93.52	5.12
4871.31	Fe I	2.87	−0.36	117.83	5.15
4872.13	Fe I	2.88	−0.56	100.27	5.05
4890.75	Fe I	2.88	−0.39	127.83	5.37
4891.49	Fe I	2.85	−0.11	131.07	5.11
4903.31	Fe I	2.88	−0.92	90.68	5.22
4918.99	Fe I	2.85	−0.34	123.67	5.19
4924.77	Fe I	2.28	−2.11	64.25	5.21
4938.81	Fe I	2.88	−1.07	73.14	5.06
4939.68	Fe I	0.86	−3.25	136.46	5.81
4946.38	Fe I	3.37	−1.17	38.09	5.20
4966.08	Fe I	3.33	−0.87	56.68	5.15
4973.10	Fe I	3.96	−0.95	9.44	4.94
4994.13	Fe I	0.92	−2.96	140.66	5.66
5001.87	Fe I	3.88	0.05	44.16	4.70
5006.11	Fe I	2.83	−0.61	104.69	5.07
5012.06	Fe I	0.86	−2.64	174.48	5.83
5014.94	Fe I	3.94	−0.30	28.89	4.84
5022.23	Fe I	3.98	−0.53	25.66	5.05
5028.12	Fe I	3.56	−1.12	16.61	4.90
5041.07	Fe I	0.96	−3.09	151.13	6.02
5041.75	Fe I	1.49	−2.20	148.85	5.80
5044.21	Fe I	2.85	−2.01	19.39	5.01
5049.82	Fe I	2.28	−1.35	122.73	5.44
5051.63	Fe I	0.92	−2.76	162.12	5.80
5060.08	Fe I	0.00	−5.46	52.39	5.45
5068.76	Fe I	2.94	−1.04	74.15	5.08

Table 6 continued

Table 6 *(continued)*

λ (Å)	Species	χ (eV)	$\log gf$	EW (mÅ)	log ϵ(X) (dex)
5074.74	Fe I	4.22	−0.20	30.14	5.11
5079.22	Fe I	2.20	−2.10	84.41	5.38
5079.74	Fe I	0.99	−3.24	141.35	6.01
5083.33	Fe I	0.96	−2.84	155.50	5.81
5098.69	Fe I	2.18	−2.03	95.76	5.49
5123.72	Fe I	1.01	−3.05	152.50	6.03
5125.11	Fe I	4.22	−0.14	28.61	5.01
5127.36	Fe I	0.92	−3.24	147.06	6.00
5131.46	Fe I	2.22	−2.51	50.68	5.30
5133.68	Fe I	4.18	0.14	52.82	5.10
5141.73	Fe I	2.42	−2.23	46.84	5.21
5142.92	Fe I	0.96	−3.08	152.70	5.99
5150.83	Fe I	0.99	−3.03	130.39	5.57
5151.91	Fe I	1.01	−3.32	141.23	6.08
5162.27	Fe I	4.18	0.02	34.92	4.92
5166.28	Fe I	0.00	−4.12	176.61	6.11
5191.45	Fe I	3.04	−0.55	115.99	5.42
5192.34	Fe I	3.00	−0.42	114.78	5.22
5194.94	Fe I	1.56	−2.02	151.43	5.68
5198.71	Fe I	2.22	−2.09	67.46	5.11
5202.33	Fe I	2.18	−1.87	105.62	5.47
5216.27	Fe I	1.61	−2.08	134.65	5.49
5217.39	Fe I	3.21	−1.16	44.93	5.07
5225.52	Fe I	0.11	−4.75	123.10	5.96
5232.94	Fe I	2.94	−0.05	136.45	5.15
5242.49	Fe I	3.63	−0.96	22.10	4.96
5247.05	Fe I	0.09	−4.94	111.61	5.92
5250.21	Fe I	0.12	−4.93	103.67	5.82
5250.64	Fe I	2.20	−2.18	85.58	5.45
5254.95	Fe I	0.11	−4.76	126.61	6.02
5263.30	Fe I	3.27	−0.87	45.31	4.87
5266.55	Fe I	3.00	−0.38	107.59	5.04
5281.79	Fe I	3.04	−0.83	76.03	5.00
5283.62	Fe I	3.24	−0.52	89.49	5.16
5302.30	Fe I	3.28	−0.72	70.81	5.10
5307.36	Fe I	1.61	−2.91	80.34	5.34
5322.04	Fe I	2.28	−2.80	21.19	5.09
5324.17	Fe I	3.21	−0.10	112.44	5.09
5328.03	Fe I	0.92	−1.46	275.72	5.75
5328.53	Fe I	1.56	−1.85	167.08	5.72
5332.90	Fe I	1.55	−2.77	96.70	5.39
5339.93	Fe I	3.27	−0.72	72.85	5.12
5364.87	Fe I	4.45	0.22	34.10	5.00
5365.40	Fe I	3.56	−1.02	14.99	4.72
5367.46	Fe I	4.42	0.44	38.56	4.84
5369.96	Fe I	4.37	0.53	50.18	4.87
5383.36	Fe I	4.31	0.64	62.39	4.87

Table 6 continued

Table 6 *(continued)*

λ (Å)	Species	χ (eV)	$\log gf$	EW (mÅ)	log ϵ(X) (dex)
5393.16	Fe I	3.24	−0.91	73.59	5.27
5410.91	Fe I	4.47	0.39	37.65	4.92
5415.19	Fe I	4.39	0.64	52.59	4.82
5424.06	Fe I	4.32	0.52	64.71	5.04
5497.51	Fe I	1.01	−2.82	163.23	5.84
5501.46	Fe I	0.96	−3.04	160.42	5.95
5506.77	Fe I	0.99	−2.78	172.42	5.92
5569.61	Fe I	3.42	−0.54	70.06	5.05
5572.84	Fe I	3.40	−0.27	88.97	5.06
5576.08	Fe I	3.43	−1.00	44.33	5.13
5586.75	Fe I	3.37	−0.14	98.95	5.04
5615.64	Fe I	3.33	0.05	129.93	5.32
5624.54	Fe I	3.42	−0.75	54.76	5.04
5658.81	Fe I	3.40	−0.79	62.36	5.15
5662.51	Fe I	4.18	−0.57	12.95	4.92
5686.52	Fe I	4.55	−0.45	6.12	4.89
5701.54	Fe I	2.56	−2.14	39.48	5.10
5753.12	Fe I	4.26	−0.68	10.54	5.03
5816.37	Fe I	4.55	−0.60	4.53	4.89
6065.48	Fe I	2.61	−1.41	89.14	5.13
6136.61	Fe I	2.45	−1.41	130.41	5.59
6137.69	Fe I	2.59	−1.34	102.84	5.25
6151.61	Fe I	2.18	−3.37	17.79	5.37
6191.558	Fe I	2.43	−1.41	124.73	5.47
6200.31	Fe I	2.61	−2.43	31.54	5.28
6213.42	Fe I	2.22	−2.48	58.47	5.25
6219.28	Fe I	2.20	−2.44	68.86	5.34
6230.72	Fe I	2.56	−1.27	119.95	5.41
6240.64	Fe I	2.22	−3.17	14.62	5.12
6246.31	Fe I	3.60	−0.87	37.17	5.05
6252.55	Fe I	2.40	−1.68	101.70	5.31
6254.25	Fe I	2.28	−2.44	62.00	5.33
6265.13	Fe I	2.18	−2.54	60.53	5.28
6301.49	Fe I	3.65	−0.71	31.46	4.85
6322.68	Fe I	2.59	−2.46	34.02	5.32
6335.33	Fe I	2.20	−2.18	81.92	5.24
6336.83	Fe I	3.69	−1.05	27.97	5.16
6344.14	Fe I	2.43	−2.87	20.72	5.26
6355.02	Fe I	2.84	−2.29	19.01	5.13
6393.60	Fe I	2.43	−1.57	108.29	5.33
6411.64	Fe I	3.65	−0.59	46.91	4.97
6421.35	Fe I	2.28	−2.01	93.84	5.34
6430.84	Fe I	2.18	−1.94	109.48	5.38
6494.98	Fe I	2.40	−1.23	133.28	5.34
6498.94	Fe I	0.96	−4.69	36.23	5.52
6592.91	Fe I	2.73	−1.47	81.04	5.17
6593.86	Fe I	2.44	−2.36	47.25	5.22

Table 6 continued

Table 6 *(continued)*

λ (Å)	Species	χ (eV)	$\log gf$	EW (mÅ)	log ϵ(X) (dex)
6609.10	Fe I	2.56	−2.66	20.37	5.17
6663.44	Fe I	2.42	−2.47	46.62	5.30
6677.98	Fe I	2.69	−1.41	97.69	5.30
6750.15	Fe I	2.42	−2.58	39.34	5.28
6978.85	Fe I	2.48	−2.45	42.64	5.26
4416.81	Fe II	2.78	−2.60	57.94	5.07
4489.18	Fe II	2.83	−2.97	29.09	4.96
4491.41	Fe II	2.86	−2.71	32.93	4.82
4520.22	Fe II	2.81	−2.60	53.63	5.01
4576.34	Fe II	2.84	−2.95	29.28	4.95
4620.52	Fe II	2.83	−3.21	17.14	4.89
4923.93	Fe II	2.89	−1.32	140.72	5.28
5018.45	Fe II	2.89	−1.22	155.56	5.38
5197.58	Fe II	3.23	−2.22	63.07	5.17
5234.63	Fe II	3.22	−2.18	64.19	5.14
5276.00	Fe II	3.20	−2.01	75.20	5.10
5284.08	Fe II	2.89	−3.19	28.97	5.15
5325.55	Fe II	3.22	−3.16	14.37	5.15
5534.83	Fe II	3.25	−2.93	28.66	5.30
6247.54	Fe II	3.89	−2.51	14.19	5.24
6432.68	Fe II	2.89	−3.71	14.07	5.21
6456.38	Fe II	3.90	−2.08	21.03	5.01
3842.04	Co I	0.92	−0.77	76.89	2.64
3845.46	Co I	0.92	0.01	122.56	2.88
4121.31	Co I	0.92	−0.32	110.45	2.73
3783.52	Ni I	0.42	−1.42	159.67	4.38
4648.65	Ni I	3.42	−0.16	14.28	3.46
4714.42	Ni I	3.38	0.23	39.62	3.59
4855.41	Ni I	3.54	0.00	20.24	3.59
4904.41	Ni I	3.54	−0.17	18.79	3.72
4980.16	Ni I	3.61	−0.11	20.79	3.79
5017.59	Ni I	3.54	−0.08	15.00	3.50
5035.37	Ni I	3.63	0.29	29.05	3.59
5080.52	Ni I	3.65	0.13	25.58	3.70
5081.11	Ni I	3.85	0.30	18.58	3.60
5084.08	Ni I	3.68	0.03	11.06	3.41
5115.40	Ni I	3.83	−0.11	16.49	3.92
5476.90	Ni I	1.83	−0.89	146.85	4.49
5578.73	Ni I	1.68	−2.64	20.87	3.87
6108.12	Ni I	1.68	−2.45	22.36	3.67
6767.77	Ni I	1.83	−2.17	47.05	3.96
4722.15	Zn I	4.03	−0.39	13.62	2.00
4810.52	Zn I	4.08	−0.13	22.25	2.06
4077.71	Sr II	0.00	0.15	···	0.42
4215.52	Sr II	0.00	−0.17	···	0.42
3600.73	Y II	0.18	0.34	···	−0.14
3601.92	Y II	0.10	−0.15	···	−0.19

Table 6 continued

Table 6 *(continued)*

λ (Å)	Species	χ (eV)	$\log gf$	EW (mÅ)	log ϵ(X) (dex)
3710.29	Y II	0.18	0.51	···	−0.24
3950.35	Y II	0.10	−0.73	···	−0.19
4398.01	Y II	0.13	−0.75	···	−0.24
4682.32	Y II	0.41	−1.73	···	−0.14
4854.86	Y II	0.99	−0.27	···	−0.38
4883.68	Y II	1.08	0.19	···	−0.19
4900.12	Y II	1.03	0.03	···	−0.02
5087.42	Y II	1.08	−0.16	···	−0.24
5119.11	Y II	0.99	−1.33	···	−0.24
5200.41	Y II	0.99	−0.47	···	−0.16
5205.72	Y II	1.03	−0.28	···	−0.19
5289.82	Y II	1.03	−1.68	···	−0.14
5473.38	Y II	1.74	−0.78	···	−0.13
3998.96	Zr II	0.56	−0.52	···	0.23
4050.32	Zr II	0.71	−1.06	···	0.53
4077.05	Zr II	0.96	−1.69	···	0.73
4149.20	Zr II	0.80	−0.04	···	0.28
4156.23	Zr II	0.71	−0.78	···	0.33
4161.20	Zr II	0.71	−0.59	···	0.28
4208.98	Zr II	0.71	−0.51	···	0.53
4317.31	Zr II	0.71	−1.45	···	0.23
4442.99	Zr II	1.49	−0.42	···	0.50
4496.96	Zr II	0.71	−0.89	···	0.38
4613.95	Zr II	0.97	−1.54	···	0.73
5112.27	Zr II	1.66	−0.85	···	0.73
3740.72	Nb II	1.62	−0.31	···	< 0.18
3864.10	Mo I	0.00	−0.01	···	< -0.17
3798.90	Ru I	0.15	−0.04	···	< 0.30
3958.86	Rh I	0.97	0.01	···	< 0.56
3404.58	Pd I	0.81	0.32	···	< 0.67
3382.89	Ag I	0.00	−0.33	···	< 0.04
3891.78	Ba II	2.51	0.29	···	−0.01
4130.65	Ba II	2.72	0.52	···	−0.02
4166.00	Ba II	2.72	−0.43	···	0.18
4524.93	Ba II	2.51	−0.39	···	0.18
5853.68	Ba II	0.60	−0.91	···	0.08
3949.10	La II	0.40	0.49	···	−0.75
3995.74	La II	0.17	−0.06	···	−0.70
4086.71	La II	0.00	−0.07	···	−0.75
4322.50	La II	0.17	−0.93	···	−0.85
4333.75	La II	0.17	−0.06	···	−0.45
4662.50	La II	0.00	−1.24	···	−0.65
4804.04	La II	0.24	−1.49	···	−0.65
4809.00	La II	0.24	−1.4	···	−0.60
4920.98	La II	0.13	−0.58	···	−0.70
4921.78	La II	0.24	−0.45	···	−0.65
4986.82	La II	0.17	−1.3	···	−0.75

Table 6 continued

Table 6 *(continued)*

λ (Å)	Species	χ (eV)	$\log gf$	EW (mÅ)	log ϵ(X) (dex)
5122.99	La II	0.32	−0.91	···	−0.45
5163.61	La II	0.24	−1.81	···	−0.65
5290.82	La II	0.00	−1.65	···	−0.65
5303.53	La II	0.32	−1.35	···	−0.75
5482.27	La II	0.00	−2.23	···	−0.75
5797.57	La II	0.24	−1.36	···	−0.45
6262.29	La II	0.40	−1.22	···	−0.55
6390.48	La II	0.32	−1.41	···	−0.45
3999.24	Ce II	0.30	0.06	···	−0.47
4073.47	Ce II	0.48	0.21	···	−0.57
4075.70	Ce II	0.70	0.23	···	−0.27
4083.22	Ce II	0.70	0.27	···	−0.37
4127.36	Ce II	0.68	0.31	···	−0.57
4137.64	Ce II	0.52	0.4	···	−0.47
4142.40	Ce II	0.70	0.22	···	−0.34
4418.78	Ce II	0.86	0.27	···	−0.57
4628.16	Ce II	0.52	0.14	···	−0.37
4882.46	Ce II	0.52	0.19	···	−0.47
5187.46	Ce II	1.53	0.17	···	−0.57
5274.23	Ce II	1.21	0.13	···	−0.47
3994.80	Pr II	1.04	−0.03	···	−0.63
4044.80	Pr II	0.06	−0.29	···	−0.73
4062.80	Pr II	0.00	0.33	···	−0.63
4189.49	Pr II	0.42	0.43	···	−0.83
4222.95	Pr II	0.06	0.23	···	−0.83
4496.33	Pr II	0.22	−0.76	···	−0.73
5135.15	Pr II	0.95	0.01	···	−0.73
5173.91	Pr II	0.97	0.36	···	−0.83
5352.40	Pr II	0.48	−0.74	···	−0.73
3838.98	Nd II	0.00	−0.24	···	−0.23
3991.74	Nd II	0.00	−0.26	···	−0.23
4004.00	Nd II	0.06	−0.57	···	−0.28
4018.82	Nd II	0.06	−0.85	···	−0.48
4023.00	Nd II	0.56	0.04	···	−0.53
4059.95	Nd II	0.20	−0.52	···	−0.43
4069.26	Nd II	0.06	−0.57	···	−0.43
4075.27	Nd II	0.06	−0.76	···	−0.33
4109.45	Nd II	0.32	0.35	···	−0.33
4177.31	Nd II	0.06	−0.1	···	−0.43
4385.66	Nd II	0.20	−0.3	···	−0.28
4462.98	Nd II	0.56	0.04	···	−0.23
4542.60	Nd II	0.74	−0.28	···	−0.33
4706.54	Nd II	0.00	−0.71	···	−0.13
4797.15	Nd II	0.56	−0.69	···	−0.48
5063.72	Nd II	0.98	−0.62	···	−0.23
5130.59	Nd II	1.30	0.45	···	−0.23
5212.36	Nd II	0.20	−0.96	···	−0.13

Table 6 continued

Table 6 *(continued)*

λ (Å)	Species	χ (eV)	$\log gf$	EW (mÅ)	log ϵ(X) (dex)
5255.51	Nd II	0.20	−0.67	···	−0.13
5311.45	Nd II	0.98	−0.42	···	−0.53
5319.81	Nd II	0.55	−0.14	···	−0.13
5356.97	Nd II	1.26	−0.28	···	−0.43
5371.93	Nd II	1.41	0.00	···	−0.43
5431.52	Nd II	1.12	−0.47	···	−0.33
5485.70	Nd II	1.26	−0.12	···	−0.25
5740.86	Nd II	1.16	−0.53	···	−0.40
4318.94	Sm II	0.28	−0.25	···	−0.39
4424.34	Sm II	0.48	0.14	···	−0.49
4434.32	Sm II	0.38	−0.07	···	−0.59
4467.34	Sm II	0.66	0.15	···	−0.49
4519.63	Sm II	0.54	−0.35	···	−0.29
4537.94	Sm II	0.48	−0.48	···	−0.49
4566.20	Sm II	0.33	−0.59	···	−0.49
4642.23	Sm II	0.38	−0.46	···	−0.49
4669.64	Sm II	0.28	−0.53	···	−0.59
5103.08	Sm II	1.16	−0.35	···	−0.49
3971.97	Eu II	0.21	0.27	···	−0.63
4129.72	Eu II	0.00	0.22	···	−0.53
4205.04	Eu II	0.00	0.21	···	−0.63
4435.58	Eu II	0.21	−0.11	···	−0.63
5966.06	Eu II	1.25	−1.04	···	−0.63
6049.51	Eu II	1.28	−0.8	···	−0.63
6173.03	Eu II	1.32	−0.86	···	−0.63
6437.64	Eu II	1.32	−0.32	···	−0.83
6645.06	Eu II	1.38	0.12	···	−0.83
7077.09	Eu II	1.25	−0.72	···	−0.83
7217.56	Eu II	1.23	−0.35	···	−0.73
7370.22	Eu II	1.32	−0.29	···	−0.71
3481.8	Gd II	0.49	0.12	···	−0.38
3796.38	Gd II	0.03	0.02	···	−0.55
4049.85	Gd II	0.99	0.48	···	−0.50
4063.38	Gd II	0.99	0.33	···	−0.40
4251.73	Gd II	0.38	−0.22	···	−0.48
4316.05	Gd II	0.66	−0.45	···	−0.38
4506.34	Gd II	0.50	−1.03	···	−0.28
3694.81	Dy II	0.10	−0.11	···	−0.35
3757.37	Dy II	0.10	−0.17	···	−0.25
3944.68	Dy II	0.00	0.11	···	−0.45
4041.98	Dy II	0.93	−0.9	···	−0.15
4050.57	Dy II	0.59	−0.47	···	−0.45
4077.97	Dy II	0.10	−0.04	···	−0.15
4103.31	Dy II	0.10	−0.38	···	−0.25
4124.63	Dy II	0.10	−0.66	···	−0.15
4129.42	Dy II	0.92	−0.61	···	−0.25
4409.38	Dy II	0.54	−1.24	···	−0.30

Table 6 continued

Table 6 *(continued)*

λ (Å)	Species	χ (eV)	$\log gf$	EW (mÅ)	log ϵ(X) (dex)
4449.70	Dy II	0.00	−1.03	···	−0.40
4620.04	Dy II	0.10	−1.93	···	−0.20
4045.45	Ho II	0.00	−0.05	···	< −0.85
3580.52	Er II	0.06	−0.62	···	−0.18
3729.52	Er II	0.00	−0.59	···	−0.53
3781.01	Er II	0.67	−0.66	···	−0.23
3786.84	Er II	0.00	−0.52	···	−0.13
3797.06	Er II	0.06	−1.03	···	−0.43
3830.48	Er II	0.00	−0.22	···	−0.83
3896.23	Er II	0.06	−0.12	···	−1.08
3795.76	Tm II	0.03	−0.23	···	−1.25
3848.02	Tm II	0.00	−0.14	···	−1.05
6221.86	Lu II	1.54	−0.76	···	< −1.05
3719.28	Hf II	0.61	−0.81	···	−0.70
3918.09	Hf II	0.45	−1.14	···	−0.80
4093.15	Hf II	0.45	−1.15	···	−0.70
3800.12	Ir I	0.00	−1.43	···	< 0.03
4057.81	Pb I	1.32	−0.22	···	< −0.20
4019.13	Th II	0.00	−0.23	···	−1.43
4094.75	Th II	0.00	−0.88	···	−1.13
4241.66	U II	0.57	−0.10	···	< −0.99